

driven by power- and time-efficient regeneration. Recently, integrating circuit switching with packet switching has been examined with the goal to create hybrid networks within individual data centers (2, 3), using optics to provide more efficient services for applications relying on large flows of data. The key insight is that by quickly reconfiguring optical paths, changes in traffic workloads can be supported. As we envision optical networking interconnecting tightly integrated rack-on-chip designs, providing both on- and off-chip connections, we need even faster optical reconfiguration and cost-effective integration to support the highly variable traffic flows between individual processors on the chip and among the chips. Next-generation data center designs built with rack-on-chip designs will need to support both circuit and packet switching.

Each processor in the rack-on-chip design must have a transceiver, consisting of a transmitter and receiver. Each processor core would be interconnected with the other cores through an optical circuit switch, which allows communication paths to be set up and reconfigured between the cores (similar to the top-of-rack switch in current data centers). The high bandwidth between processor cores will require using both spatial and spectral (wavelengths) degrees of freedom, with wavelength-division multiplexing. Pairing each processor core with a transceiver requires miniaturizing transceivers and integrating them with the rack-on-chip design. The transceiver should be low-power and highly efficient, meaning that excessive heat is not generated, and that only a small number of photons over relatively short distances should be necessary to represent a bit of information, transmitted with low loss, and detected with an efficient receiver.

Nanophotonic technologies may meet the requirements for miniaturizing transceivers and circuit switches, using metamaterials, resonant nanostructures, nanoscale lasers, modulators, and receivers and switches. For example, it is possible to use advanced lithography to write and assemble devices and circuits into subsystems that support the rack-on-chip design. Recent advances in silicon photonics using complementary metal-oxide semiconductor-compatible manufacturing processes (4) mean that chip-scale, highly integrated optoelectronic solutions can be realized at low cost while meeting the other needs of scalability, bandwidth, fault tolerance, and energy efficiency. However, the efficient generation of light on a silicon chip is still in its infancy, and may not be able to overcome the fundamental issues prohibiting efficient generation

of light in indirect band-gap semiconductors. Alternative solutions similar to the delivery of electrical power from off-chip sources will bring the optical fields into the rack-on-chip. Or photons can be generated on the chip—for example, through heterogeneous integration of III-V compound semiconductor devices, such as nanolasers (5, 6).

To achieve highly scalable optical circuit architectures that can support many processor cores, each switching element must be miniaturized, relying on high optical nonlinearities that are very difficult to achieve in natural materials. One approach could be to develop nonlinear metamaterials, which are deeply subwavelength composites, engineered on atomic scale and/or a scale of a few atomic layers, exhibiting a qualitatively different response to radiation than that predicted by the effective medium theories of classical physics (e.g., crystal symmetry breaking, exotic semimetal modulation materials, and composite metal-dielectric nonlinear materials). The high nonlinear coefficient of new nonlinear metamaterials together with small-volume localized modes will enable low energy-per-bit operation.

Once this optical networking technology is integrated with electronic proces-

sors as a rack-on-chip design, the number of such chips can then be scaled up to meet the needs of future data centers. This will enable delivering new kinds of applications, such as computational climate modeling and biological applications, big data applications harnessing huge data sets, and online applications delivered to hundreds of millions of users.

#### References and Notes

1. M. Asghari, A. Krishnamoorthy, *Nat. Photon.* **5**, 268–270 (2011).
2. N. Farrington *et al.*, in *Proceedings of the ACM 2010 SIGCOMM Conference*, New Delhi, India, 30 August to 3 September 2010 (Association for Computing Machinery, New York, 2010), pp. 339–350.
3. G. Wang *et al.*, in *Proceedings of the ACM 2010 SIGCOMM Conference*, New Delhi, India, 30 August to 3 September 2010 (Association for Computing Machinery, New York, 2010), pp. 327–338.
4. "Luxtera, Freescale collaborate on CMOS photonics fab," <http://optics.org/article/39426>, 9 June 2009.
5. M. P. Nezhad *et al.*, *Nat. Photon.* **4**, 395–399 (2010).
6. M. Khajavikhan *et al.*, *Nature* **482**, 204–207 (2012).

**Acknowledgments:** Supported by the Google Focused Research Award, the Defense Advanced Research Projects Agency, NSF, NSF Engineering Research Center for Integrated Access Networks, the Office of Naval Research, the Cymer Corporation, the U.S. Army Research Office, and the UCSD Center for Networked Systems.

10.1126/science.1242906

#### DEVELOPMENT

## Getting Your Gut into Shape

Benjamin D. Simons<sup>1,2,3</sup>

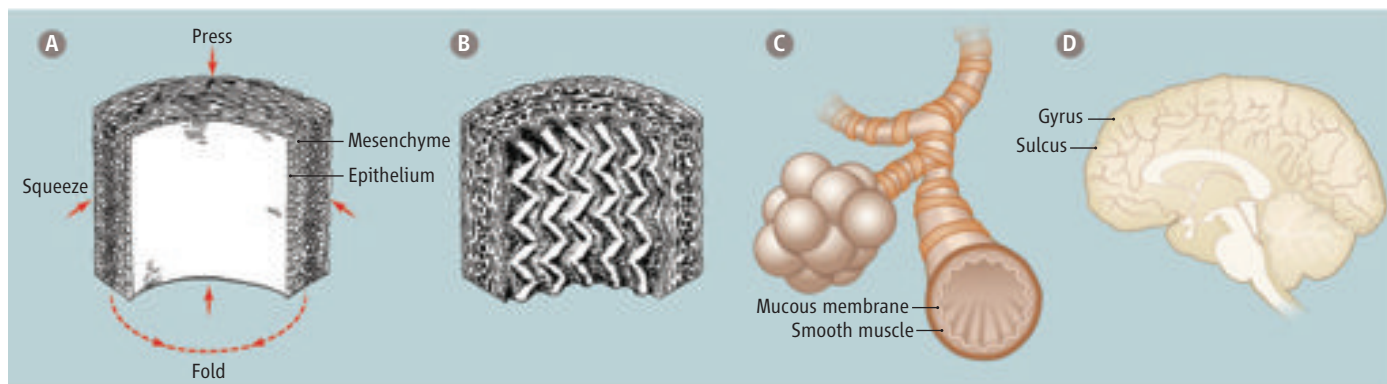
Mechanical forces exerted between tissue layers in the intestine are all that is needed to make gut villi.

The specification and patterning of plant and animal tissues relies upon the spatial and temporal coordination of biochemical and physical processes at the molecular, cellular, and tissue scale (1, 2). Yet, despite access to genetic manipulation techniques and in vivo live-imaging platforms, progress in understanding how these processes interact in development has proved challenging. Reliant on the interplay of gene regulatory and mechanical cues, the emergence of spatial organization in the gut epithelium provides a paradigm for morpho-

genic processes in vertebrates. On page 212 of this issue, Shyer *et al.* (3) combine in vitro analyses of tissue explants with the development of a biophysical modeling scheme to show that the seemingly complex process of intestinal villi specification can be explained simply through the action of mechanical constraints.

In vertebrates, the digestive tract arises from a primitive gut tube (4). As the gut matures, the foregut, midgut, and hindgut become morphologically distinct, before differentiating into specialized primary organs: The foregut (pharynx, esophagus, and stomach) is responsible for ingestion and the initiation of digestion, whereas the midgut (small intestine) provides the major site of digestion and nutrient absorption, and the hindgut (large intestine) resorbs water and expels waste. To fulfill these functions, the

<sup>1</sup>Cavendish Laboratory, Department of Physics, J. J. Thomson Avenue, University of Cambridge, Cambridge CB3 0HE, UK. <sup>2</sup>The Wellcome Trust/Cancer Research UK Gurdon Institute, University of Cambridge, Tennis Court Road, Cambridge CB2 1QN, UK. <sup>3</sup>Wellcome Trust-Medical Research Council Stem Cell Institute, University of Cambridge, UK. E-mail: bds10@cam.ac.uk



gut organ epithelia acquire distinct luminal morphologies (5). In particular, to maximize the absorptive area of the epithelium, the mucosa of the small intestine is remodeled into an intricate array of finger or leaf-like protrusions, known as villi, which extend into the lumen. At the base of the villi, smaller glands, known as crypts of Lieberkühn, form invaginations that open onto the luminal surface and provide a niche environment for the stem cells that support the rapid turnover of the epithelium (6).

For many organisms, the morphology of the small intestine is not specified directly through a genetically determined developmental program but instead emerges in a sequence of morphological alterations (5, 7). This stepwise progression is exemplified by the chick: Early in development, the small intestine comprises a smooth cylinder of mesenchyme, supported by an external layer of mesothelium and an internal layer of epithelium (see the figure, panel A). As the epithelium expands by cell division and the mesenchyme differentiates to form a layer of circularly oriented smooth muscle, a regular array of “previllous” ridgelike structures develops along the length of the gut. Later, two further layers of longitudinal smooth muscle appear sequentially on either side of the circular muscle, the first accompanied by a transition of the ridges into a herringbone pattern of zigzags (see the figure, panel B) and the second leading to the emergence of villi. Finally, late in development, crypts form following the specification of progenitors at the base of the villi, which form invaginations into the submucosa.

Previous studies have conjectured that mechanical factors might drive morphogenesis in the intestine (5, 7, 8). However, the question of whether patterning emerges “passively” from the resolution of mechanical stresses imposed by the expansion of the epithelium against the muscle layer, or whether it results from the active contraction of individual cells, remained open. By designing a combination of in vitro assays, Shyer *et al.* show

that the emergence of previllous structures in the chick embryo relies on mechanical constraints imposed by muscle differentiation. As well as demonstrating that the separation of the muscle layer from the internal mesenchyme and epithelium inhibits the formation of ridgelike structures in vitro, they show that patterning can be restored simply by constraining the circumferential expansion of the muscle-free gut using a porous silk tube. Similarly, they have shown that the subsequent “buckling” of the ridges can be abolished by chemically inhibiting the first round of longitudinal muscle differentiation, whereas inhibition of the second round prevents transformation of the zigzag pattern into villi.

To further elucidate the dynamic process of remodeling, Shyer *et al.* develop a minimal biophysical modeling scheme, based only on the minimization of the strain energy of the layered structure, treating the growing tissue as a geometrically constrained elastic material. Within this scheme, they provide a quantitative basis for the origin and scale of the sequence of alterations and, through adjustments in the constitutive parameters, account for the diverse range of villi structures seen in different organisms, from *Xenopus* and zebrafish to snakes and mice.

Numerous studies have emphasized the importance of differential growth and mechanical stress in shaping the morphology of multicellular organisms and tissues (9–11). Patterning in airways (12), arteries (13), skin (14), and brain (15) have all been associated with buckling-like instabilities created by mechanical forces acting on a growing tissue (see the figure, panels C and D). The present study provides a firm experimental basis for mechanics not just contributing to, but driving, patterning in the intestinal epithelium.

In the light of this work, it is natural to question whether the final stage of intestinal patterning, the invagination of crypts, can also be accounted for by mechanical forces. However, the remarkable ability of individual intestinal stem cells to reconstitute organized

**Tissue “origami” builds gut villi.** Expansion of the growing epithelium in the small intestine of vertebrates against layers of muscle in the mesenchyme (A) leads to buckling and the progressive emergence of patterned fingerlike structures known as villi (B) [after (7)]. A similar buckling mechanism is thought to account for the appearance of textures in a variety of layered tissues from (C) the folds in the mucosal lining of the bronchioles in lung to (D) the convoluted structures of the cerebral cortex in large mammals.

cryptlike structures in vitro, in the absence of an underlying mesenchyme (16), points to a different mechanism where transcriptional regulation and cell-cell interactions conspire with mechanical cues to engineer a stereotyped cellular organization.

In the postgenomic era, it has become anathema to speak about “mechanism” without reference to interactions of genes and gene products. The current study is instructive in that, without addressing information on subcellular processes, it fulfills the objective of mechanistic understanding, providing an explanation of the emergence of patterning and offering predictive new insights.

## References

1. C. T. L. Wolpert, *Principles of Development* (Oxford Univ. Press, Oxford, 4th ed., 2011).
2. C.-P. Heisenberg, Y. Bellaïche, *Cell* **153**, 948 (2013).
3. A. E. Shyer *et al.*, *Science* **342**, 212 (2013).
4. A. M. Zorn, J. M. Wells, *Annu. Rev. Cell Dev. Biol.* **25**, 221 (2009).
5. W. A. Hilton, *Am. J. Physiol.* **1**, 459 (1902).
6. H. Clevers, *Cell* **154**, 274 (2013).
7. A. J. Coulombre, J. L. Coulombre, *J. Embryol. Exp. Morphol.* **6**, 403 (1958).
8. D. R. Burgess, *J. Embryol. Exp. Morphol.* **34**, 723 (1975).
9. D. W. Thompson, *On Growth and Form* (Cambridge Univ. Press, Cambridge, 1942).
10. L. A. Taber, *Appl. Mech. Rev.* **48**, 487 (1995).
11. J. Dervaux, M. Ben Amar, *J. Mech. Phys. Solids* **59**, 538 (2011).
12. R. K. Lambert *et al.*, *J. Appl. Physiol.* **77**, 1206 (1994).
13. A. Goriely, R. Vandiver, *IMA J. Appl. Math.* **75**, 549 (2010).
14. M. Kücken, A. C. Newell, *J. Theor. Biol.* **235**, 71 (2005).
15. D. P. Richman *et al.*, *Science* **189**, 18 (1975).
16. T. Sato, H. Clevers, *Science* **340**, 1190 (2013).

10.1126/science.1245288



# Villification: How the Gut Gets Its Villi

Amy E. Shyer,<sup>1\*</sup> Tuomas Tallinen,<sup>2,3\*</sup> Nandan L. Nerurkar,<sup>1</sup> Zhiyan Wei,<sup>2</sup> Eun Seok Gil,<sup>4</sup> David L. Kaplan,<sup>4</sup> Clifford J. Tabin,<sup>1†</sup> L. Mahadevan<sup>2,5,6,7,8†</sup>

The villi of the human and chick gut are formed in similar stepwise progressions, wherein the mesenchyme and attached epithelium first fold into longitudinal ridges, then a zigzag pattern, and lastly individual villi. We find that these steps of villification depend on the sequential differentiation of the distinct smooth muscle layers of the gut, which restrict the expansion of the growing endoderm and mesenchyme, generating compressive stresses that lead to their buckling and folding. A quantitative computational model, incorporating measured properties of the developing gut, recapitulates the morphological patterns seen during villification in a variety of species. These results provide a mechanistic understanding of the formation of these elaborations of the lining of the gut, essential for providing sufficient surface area for nutrient absorption.

In amniotes, the primitive midgut is established as a cylinder with an outer mesenchymal layer and an inner, luminal endoderm. As development proceeds, distinct radial layers of smooth muscle differentiate. In parallel, the luminal surface of the gut transforms from a smooth surface to a convoluted morphology. In humans, as well as in mice and birds, this leads to an organized array of fingerlike projections termed intestinal villi (1, 2) although a variety of morphologies such as

ridges, zigzags, and honeycombs occur in other species (3–5). Early work suggested a mechanical basis for villus formation (6); however, systematic biological or physical studies of this hypothesis are lacking.

## Morphogenesis and Differentiation of the Chick Midgut

Until embryonic day 7 (E7), the gut tube, with its inner endodermally derived epithelium and outer

mesenchymal layer, maintains a smooth luminal surface (Fig. 1A). At E8, as the first layer of circumferentially oriented smooth muscle begins to form, inward buckling of the tube leads to longitudinal ridges that increase in number until E13, when the differentiation of this layer is complete (Fig. 1B). At this point, a second longitudinally oriented layer of muscle differentiates just exterior to the circular layer, while the previously formed ridges fold into parallel zigzags over 3 days (Fig. 1C). Last, at E16, as a third longitudinally oriented muscle layer differentiates just interior to the circular layer, bulges arise from the

<sup>1</sup>Department of Genetics, Harvard Medical School, Boston, MA 02115, USA. <sup>2</sup>School of Engineering and Applied Sciences, Harvard University, Cambridge, MA 02138, USA. <sup>3</sup>Department of Physics and Nanoscience Center, University of Jyväskylä, FI-40014 Jyväskylä, Finland. <sup>4</sup>Department of Biomedical Engineering, Tufts University, Medford, MA 02155, USA. <sup>5</sup>Department of Organismic and Evolutionary Biology, Harvard University, Cambridge, MA 02138, USA. <sup>6</sup>Department of Physics, Harvard University, Cambridge, MA 02138, USA. <sup>7</sup>Wyss Institute for Biologically Inspired Engineering, Harvard University, Cambridge, MA 02138, USA. <sup>8</sup>Kavli Institute for Nanobio Science and Technology, Harvard University, Cambridge, MA 02138, USA.

\*These authors contributed equally to this work.

†Corresponding author. E-mail: lm@seas.harvard.edu (L.M.); tabin@genetics.med.harvard.edu (C.J.T.)

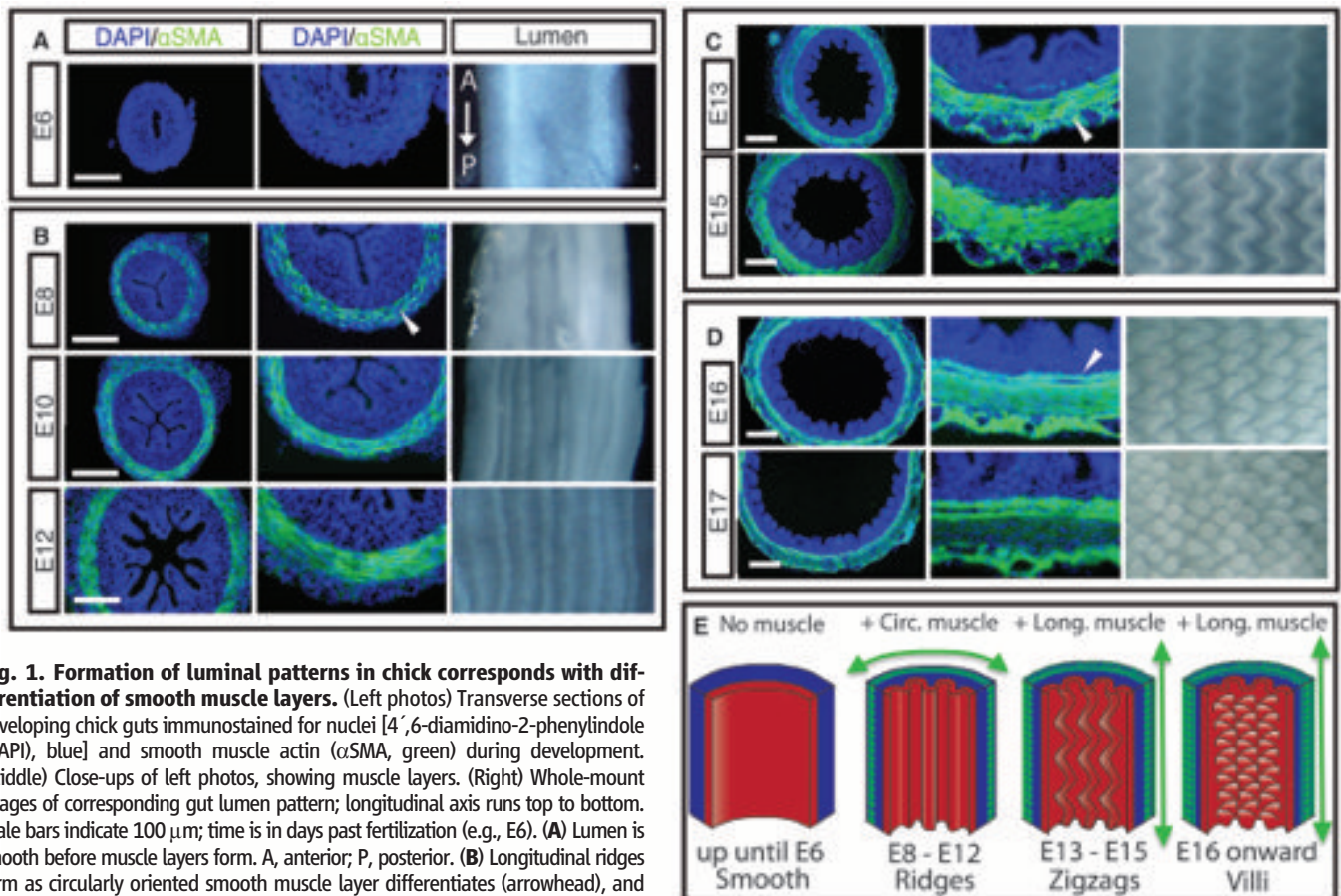


**Fig. 1. Formation of luminal patterns in chick corresponds with differentiation of smooth muscle layers.** (Left photos) Transverse sections of developing chick guts immunostained for nuclei [4',6-diamidino-2-phenylindole (DAPI), blue] and smooth muscle actin ( $\alpha$ SMA, green) during development. (Middle) Close-ups of left photos, showing muscle layers. (Right) Whole-mount images of corresponding gut lumen pattern; longitudinal axis runs top to bottom. Scale bars indicate 100  $\mu$ m; time is in days past fertilization (e.g., E6). (A) Lumen is smooth before muscle layers form. A, anterior; P, posterior. (B) Longitudinal ridges form as circularly oriented smooth muscle layer differentiates (arrowhead), and ridge number increases as this layer develops. (C) Longitudinal muscle develops exterior to the circular layer (arrowhead) coincident with the formation of zigzags whose periodicity is maintained but with increasing amplitude and compactness over time. (D) A second longitudinal muscle layer forms, interior to the circular layer (arrowhead), coincident with the formation of villi. (E) Schematic illustrating the process of muscle differentiation and luminal patterning over time.

(E) Schematic illustrating the process of muscle differentiation and luminal patterning over time. The diagram shows four stages: 1. 'up until E6 Smooth' (a simple tube), 2. 'E8 - E12 Ridges' (a tube with longitudinal ridges), 3. 'E13 - E15 Zigzags' (a tube with zigzagging ridges), and 4. 'E16 onward Villi' (a tube with finger-like villi). Arrows indicate the progression from left to right.

zigzag pattern that presage the formation of villi (Fig. 1D). The coincident emergence of luminal ridges, zigzags, and villi with the sequential formation of smooth muscle layers suggests that smooth muscle differentiation and epithelial morphogenesis might be linked.

### Ridges Form Because of Muscle-Constrained Azimuthal Growth of the Endoderm-Mesenchyme Composite

The notion that differential growth of layered tissues can lead to epithelial buckling is classical (7, 8) and has been evoked, for example, to explain longitudinal ridge formation in healthy and diseased adult trachea and esophagus (4, 9). To investigate the tissue interactions that lead to the ridge patterns in the embryonic gut, we surgically separated the layers and observed the effects on their respective morphologies. When the muscle was separated from the combined mesenchymal and epithelial layers at different stages from E8, when the circular muscle layer first forms, to E12 just before the first longitudinal muscle layer forms, we found that the mesenchyme and attached epithelium unfold (Fig. 2A). This indicates that relative growth of these layers leads to reversible elastic compression when constrained within the muscle layer; indeed the ratio of the inner circumference of the once-attached muscle layer to the outer circumference of the separated mesenchyme and endoderm, the circumferential stretch ratio, consistently averages to 0.55 across the developmental stages from E8 to E12 (Fig. 2B). However, the separation of the endoderm from the composite of mesenchyme and muscle does not abolish ridge pattern in the mesenchyme (Fig. 2C).

Taken together, these results support a model that the circular muscle layer, once differentiated, forms a stiff constraint mechanically preventing the free azimuthal expansion of the mesenchyme and endoderm; further growth of these tissues relative to the muscle layer leads to azimuthal compression and buckling. This suggests that absent muscle differentiation, the gut tube would expand freely radially without ridge formation. To test this, we developed an in vitro culture system for gut growth. When segments of E6 guts with smooth lumens and no muscle layers were cultured for 48 hours in vitro, they differentiated to form a ring of circumferential smooth muscle and parallel luminal folds, indistinguishable from in ovo E8 guts (Fig. 2D). When E6 guts were cultured in the presence of 10  $\mu$ M AG1295 or FK506, drugs known to block the differentiation of smooth muscle but that act through distinct signaling pathways (10, 11), they did not form a smooth muscle layer and concomitantly did not form luminal folds (Fig. 2D). Importantly, these compounds did not influence proliferation or lead to an increase in cell death when compared with guts grown with the vehicle (dimethyl sulfoxide, DMSO) alone (fig. S1); indeed there was a significant increase in the outer circumference of guts lacking circular smooth muscle when com-

pared with control gut samples, confirming that blocking smooth muscle differentiation eliminates circumferential restriction of the outward expansion of the gut tube. As a control, gut segments grown in vehicle alone developed a layer of circular smooth muscle and formed luminal folds. Quantifying the constraint provided by the muscle, we find that the ratio of inner circumference of the muscle layer in the control samples to the outer circumference of the gut segments cultured

with either compound to be 0.53 on average (Fig. 2D), a ratio that agrees closely with the stretch ratio obtained from surgical separation of the layers, indicating that tissue differentiation into smooth muscle provides most of the circumferential constraint.

Because smooth muscle begins active peristalsis once it forms, the contractility of muscle could drive epithelial buckling in addition to, or instead of, functioning as a passive barrier to expansion. To test this, we cultured E6 gut segments

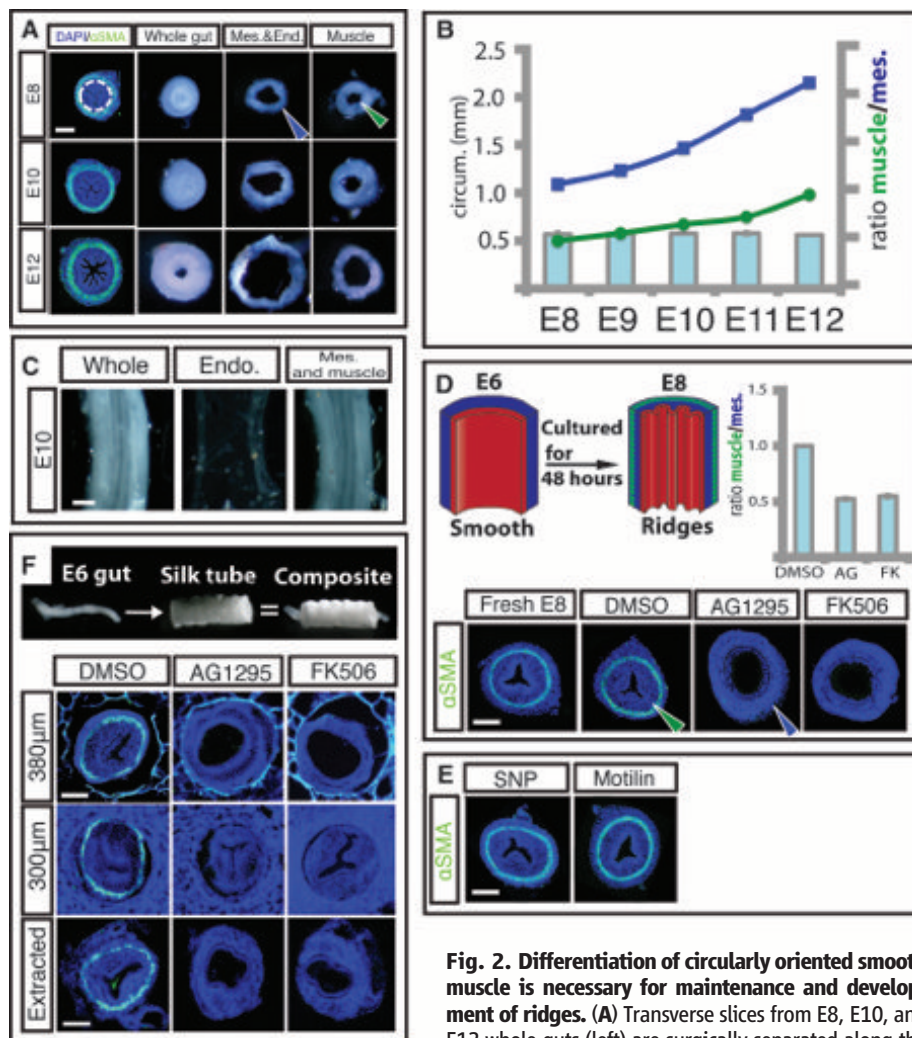


**Fig. 2. Differentiation of circularly oriented smooth muscle is necessary for maintenance and development of ridges.** (A) Transverse slices from E8, E10, and E12 whole guts (left) are surgically separated along the junction of the mesenchyme and the circular smooth

muscle (dotted line). When separated from the muscle, the luminal ridges in the mesenchyme and attached endoderm unfold (middle) and expand, whereas the detached muscle remains invariant (right). The outer circumference of the unfolded mesenchyme and endoderm (blue arrowhead) is larger than the inner circumference of the separated muscle layer (green arrowhead). (B) Inner circumference of muscle layer (green line) compared with outer circumference of mesenchyme and endoderm (blue line) over time, along with the compression ratio (bar graph). (C) Surgical separation of endoderm from mesenchyme and muscle at E10 does not abolish ridge pattern. (D) (Top left) Experiment schematic of E6 gut cultured for 48 hours. (Bottom) Transverse sections of a fresh E8 gut or E6 guts cultured in DMSO alone or with either 10  $\mu$ M AG1295 or 10  $\mu$ M FK506 for 48 hours and labeled with DAPI (blue) and SMA (green). (Top right) Quantification of compression from E8 muscle shows the ratio of the inner circumference of the circular muscle at E8 (green arrowhead) to the resulting mesenchyme outer circumference (blue arrowhead). (E) Transverse sections of guts labeled as in (D); culturing E6 guts in the presence of either SNP or motilin does not affect ridge formation. (F) Transverse sections of guts labeled as in (D), cultured in silk tubes of 380- $\mu$ m inner diameter (top) or 300- $\mu$ m inner diameter (middle) or cultured in 300  $\mu$ m and extracted before fixation (bottom).  $n > 3$  for all culture experiments; error bars represent one SD. Scale bars = 100  $\mu$ m.



with either sodium nitroprusside (SNP), a compound shown to inhibit smooth muscle contraction during peristalsis, or motilin, known to enhance peristaltic smooth muscle contraction (12, 13). After 48 hours in culture, neither compound affected the formation of luminal ridges, suggesting that the spontaneous contractility of smooth muscle is not required for epithelial buckling (Fig. 2E).

Last, to assess whether the role of the circular smooth muscle layer as a stiff barrier is sufficient to drive luminal folds, we sought to mimic its role in samples where smooth muscle development was blocked. To do so, we constrained radial gut growth by using porous silk tubes, synthesized by spinning silk fibroin around a reciprocating rotating mandrel with the inner diameter of the circular smooth muscle (14). E6 gut segments cultured inside of silk tubes in the presence of either AG1295 or FK506 for 48 hours did not form a muscle layer and, when given sufficient room to expand in silk tubes of 380- $\mu$ m inner diameter, still did not form luminal ridges (Fig. 2F). However, when the segments were grown in AG1295 and FK506 and restricted by a silk tube of inner diameter of 300  $\mu$ m, they formed ridges similar to those seen in control guts in spite of the lack of smooth muscle (Fig. 2F). This demonstrates that the mechanical barrier function of the circumferential smooth muscle is sufficient for luminal ridge formation. Moreover, upon removal from the confining silk tube, these ridges were quickly lost, just as they vanished from gut tubes upon surgical removal of the circumferential muscle layer (Fig. 2F), corroborating our previous finding that continued mechanical constraint is required for the maintenance of luminal ridges.

### Zigzag Intermediates Form in Response to Additional Muscle-Constrained Longitudinal Growth in Endoderm-Mesenchyme Composite

As described earlier, at E13 a second longitudinally oriented muscle layer forms; simultaneously the ridges buckle into zigzags. Previous work has shown that a thin layer atop an elastic substrate may take on a zigzag topography when it is compressed biaxially (15–17), suggesting that the longitudinal muscles in conjunction with the previously established circumferential muscle compress the gut biaxially. To investigate whether the longitudinal muscle layer generates longitudinal compression, we surgically separated the muscle layers from the endoderm-mesenchyme composite at different developmental stages. At E12, before longitudinal muscle or zigzags have formed, the separated mesenchyme and attached endoderm have about the same axial length as the muscle to which they were attached (Fig. 3A). However, after longitudinal muscle layer differentiation, at E13, E14, and E15, the ratios of the length of separated muscle to the mesenchyme and endoderm were about 0.75, 0.69, and 0.55, respectively (Fig. 3A), showing that the endoderm-mesenchyme is increasingly compressed longitudinally as this muscle layer forms. Conversely, separation of the endoderm from the

mesenchyme and muscle at E14 did not abolish the zigzag pattern, suggesting that this interaction is not required for maintenance of the zigzags (Fig. 3B).

To directly test whether the development of the outer longitudinal layer is required for the formation of zigzags, we resorted again to our *in vitro* culture system. When E12 gut segments, with a single, circumferential smooth muscle layer and parallel ridges, were cultured for 48 hours, they differentiated a longitudinal smooth muscle layer and underwent morphogenesis to form zigzags, similar to those seen in guts harvested at E14 (Fig. 3C). In the presence of either AG1295

or FK506, the longitudinal muscle layer failed to differentiate, and concomitantly the zigzag pattern did not form, suggesting that the longitudinal layer is required to induce zigzags. These compounds only block further smooth muscle formation and leave established layers intact, so the ridge patterns remain (Fig. 3C). Additionally, when differentiation of this longitudinal muscle was blocked, the length of the gut increased significantly compared with control gut segments; the ratio of the length of control gut segments to those cultured in the presence of either compound was on average 0.66; that is, this longitudinal muscle layer compressed the mesenchyme and attached

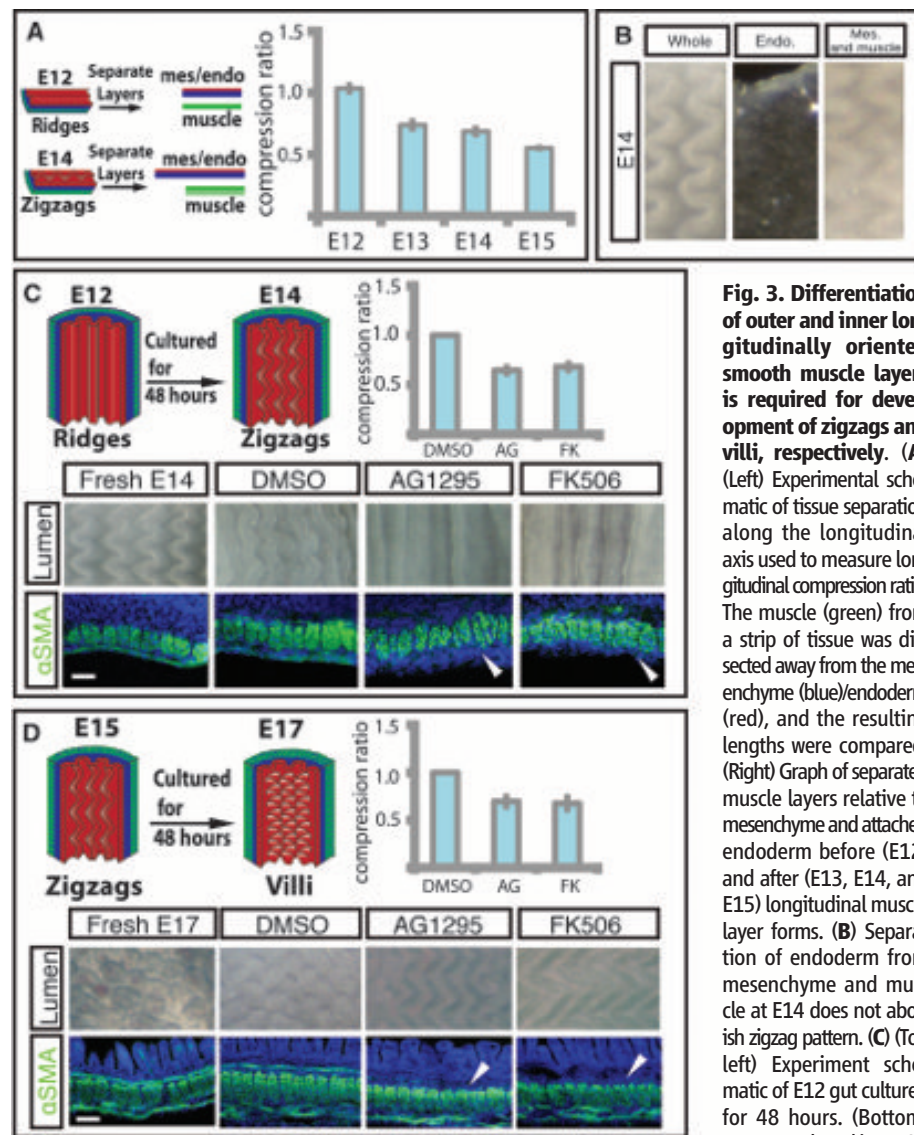


**Fig. 3. Differentiation of outer and inner longitudinally oriented smooth muscle layers is required for development of zigzags and villi, respectively.** (A) (Left) Experimental schematic of tissue separation along the longitudinal axis used to measure longitudinal compression ratio. The muscle (green) from a strip of tissue was dissected away from the mesenchyme (blue)/endoderm (red), and the resulting lengths were compared. (Right) Graph of separated muscle layers relative to mesenchyme and attached endoderm before (E12) and after (E13, E14, and E15) longitudinal muscle layer forms. (B) Separation of endoderm from mesenchyme and muscle at E14 does not abolish zigzag pattern. (C) (Top left) Experiment schematic of E12 gut cultured for 48 hours. (Bottom) E12 guts cultured in DMSO

alone or with either 10  $\mu$ M AG1295 or 10  $\mu$ M FK506 for 48 hours. Middle photos show luminal views, and bottom photos show longitudinal sections labeled with DAPI (blue) and SMA (green). Arrowheads denote absence of muscle layer. (Top right) Quantification of compression from E14 longitudinal muscle characterized by the ratio of the length of the control cultured segments to those lacking muscle. (D) (Top left) Experiment schematic of E15 gut cultured for 48 hours. (Bottom) Fresh E17 gut or E15 guts cultured in DMSO alone or with either 10  $\mu$ M AG1295 or 10  $\mu$ M FK506 for 48 hours. Middle photos show luminal views and bottom photos show longitudinal sections, labeled as in (C). Arrowheads denote absence of muscle layer. (Top right) Quantification of compression from E16 longitudinal muscle, as in (C).  $n > 3$  for all culture experiments; error bars represent one SD. Scale bars = 20  $\mu$ m.

epithelium by a factor of about 1.5 (Fig. 3C). This is consistent with the value obtained by manual dissection of the layers. Just as for ridge formation, transformation of ridges to zigzags is independent of smooth muscle contractility (fig. S2).

### Villification Requires a Third Regime of Smooth Muscle Differentiation

To investigate the dependence of the final patterning of villi on the differentiation of the inner, longitudinal smooth muscle layer, we cultured E15 guts, with both a circumferential layer and outer longitudinal layer, for 48 hours in the presence of the muscle-blocking compounds or with the vehicle (DMSO) alone. Although gut segments cultured with DMSO developed a third inner longitudinal muscle layer and formed villi, those cultured with either AG1295 or FK506 failed to form this muscle layer and did not initiate villi (Fig. 3D). When differentiation of this longitudinal muscle was blocked, the length of the tube increased significantly compared with those of control gut segments (Fig. 3D). The ratio of the length of control gut segments to that of those lacking the outer longitudinal muscle was on average 0.68; that is, this muscle layer compressed the mesenchyme and endoderm again by a factor of about 1.5 (Fig. 3D).

All together, our surgical manipulations and drug studies support the hypothesis that differentiating smooth muscle acts as a barrier to the expansion of the attached mesenchyme and endoderm, compressing these layers first circumferentially to form ridges, then longitudinally to form zigzags, and last longitudinally again to form villi. We emphasize that, because the patterns relax when the muscular constraints are released surgically, it follows that the morphology of the lumen is a simple consequence of elastic energy minimization during the constrained growth of a soft, layered elastic tissue.

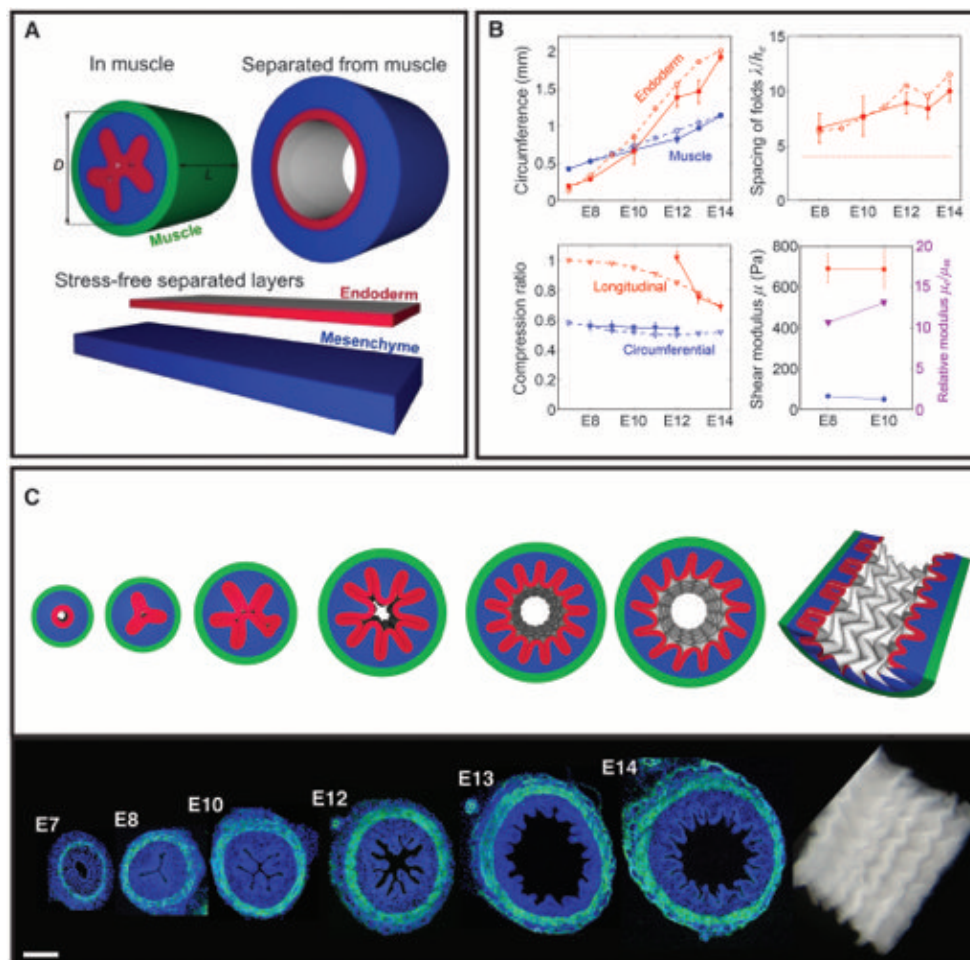
### Mathematical Models Quantify the Role of Tissue Growth Constrained by Muscle Layers to Drive Ridge and Zigzag Formation

To further quantify these luminal patterns, we constructed a mathematical and computational model of the process based on measured geometrical and biophysical parameters. Our models are similar in spirit to recent theoretical approaches to gut luminal patterning based on the hypothesis of differential growth (*18, 19*) but go beyond them by correctly accounting for the constraints provided by the combination of muscular differentiation and differential growth that we see evidence for, the cylindrical geometry of the gut, and the

experimentally measured geometrical and physical properties of the system.

We start by considering a composite of naturally flat elastic mesenchyme and endoderm sheets that are attached together and bent and squeezed to fit into a rigid tubular configuration of inner diameter  $D$  that mimics the circular muscle layer (Fig. 4A). We assume that the tissues may be well described by using a simple neo-Hookean constitutive model, with a volumetric strain energy density  $W = \frac{1}{2}\mu[\text{Tr}(\mathbf{F}\mathbf{F}^T)J^{-2/3} - 3] + K(J - \log J - 1)$ , where  $\mu$  and  $K$  are the shear and bulk moduli, respectively;  $\mathbf{F}$  is the elastic deformation gradient; and  $J = \det(\mathbf{F})$ . Over the multiday time scale of villification, the tissues are assumed compressible with  $K = 3\mu$ . At each stage, we minimize the elastic energy of the system by using a custom finite element model (supplementary materials). We characterize growth by using the experimentally measured growth parameters, including the outer circumference,  $S_0 = \pi D$ , of the compressed endoderm-mesenchyme composite, as well as the circumference and thickness of the endoderm and mesenchyme (Fig. 4B and fig. S7). The simulated domain has length  $L = 1.25D$  in the longitudinal direction with periodic boundary conditions at the ends, allowing uniform relative longitudinal growth of the layers to develop

**Fig. 4. A numerical simulation predicts the formation of ridges and zigzags in chick gut lumen.** (A) The model is illustrated by showing the mesenchyme (blue) and the endoderm (red) enclosed in a muscle (green), without muscle, and separated in their stress-free states. (B) (Top left) Circumference of the inner boundary of the muscle and endoderm. (Top right) Spacing of longitudinal folds measured along the endoderm and scaled by its thickness. The thin dashed line is the stress-free thickness of the endoderm-mesenchyme composite. (Bottom left) Ratio of muscle to separated endoderm-mesenchyme composite in circumferential and longitudinal directions. (Bottom right) Shear modulus of mesenchyme and endoderm, and their ratio. In all graphs, solid lines correspond to experimental observations and dashed lines to the computational model. Error bars, 1 SD. (C) A simulation shows ridge-folds forming due to circumferential compression, followed by buckling into a zigzag pattern due to longitudinal compression. Sections of corresponding chick guts labeled with DAPI (blue) and SMA (green) are shown below.





axial compression that mimics the role of the longitudinal muscles at E13 and E14 when zigzags arise. With the geometrical parameters (full details in the supplementary materials) and the measured elastic moduli of the tissues (Fig. 4B and figs. S3 to S6) that show that the endoderm is about 10 times stiffer than the mesenchyme, our simulations allow us to follow the evolution of luminal patterning shown in Fig. 4C and movie S1. We see that both ridge and zigzag patterns arise as mechanical instabilities in the constrained growing tissue that sequentially break circumferential and then longitudinal symmetry in the gut with a wavelength and amplitude comparable to the thickness of the endoderm-mesenchyme composite (Fig. 4B).

### Villification Also Requires Localized Changes in Endodermal and Mesenchymal Proliferation in Addition to Smooth Muscle Differentiation

Although additional compression from the inner longitudinal layer is necessary for the formation of villi from zigzags, as shown in Fig. 3, longitudinal compression alone is not sufficient to effect this transformation (fig. S9A).

Previous work in mouse has shown that, although proliferating cells can be found uniformly across the mesenchyme and endoderm before villi arise, as villi form, proliferating cells are found only in the intervillous region (2). Similarly, in chick guts, proliferating cells appear uniformly within each tissue layer through the formation of zigzags (Fig. 5 and fig. S8), but at E15, after zigzags form and just before villi arise, proliferating cells are found predominantly in the valleys between the raised zigzags (Fig. 5A). However, once villi begin to form at E16, proliferation is no longer restricted from the tips (Fig. 5A). Additionally we find that *in vitro* 5-ethynyl-2'-deoxyuridine (EdU) pulse labeling of E15 gut samples results in labeled cells at the sides and tips of forming villi, suggesting that these changes in proliferation patterns may reflect a displacement of the dividing cells upward from the valleys as the luminal topography shifts from zigzags to villi. Specifically, each "arm" of the zigzag twists out of the plane and into the lumen, pinching off a region of the zigzag arm near each "elbow," delineating pockets of mesenchyme surrounded by endoderm, each of which becomes a villus (Fig. 5B).

To understand how the topographical changes during zigzag twisting might relocate regions of proliferation as villi form, we created a clay model of zigzags. Labeling the proliferating regions of our model zigzags and manually twisting them mimics the twist observed in the E16 gut (Fig. 5C). Furthermore, the resulting clay label localization closely matches EdU staining for proliferation in the sectioned E16 gut tissue (Fig. 5C), suggesting that these tissue movements account for the observed proliferation patterns as villi form.

To probe the effect of nonuniform growth in our computational model, we set up a minimal planar configuration of mesenchyme and endo-

derm (supplementary materials, fig. S9, and movie S2). Initially, the endoderm and mesenchyme are assumed to have nominal compression ratios of 0.5 and 0.6, respectively, in both lateral directions, as measured experimentally (Fig. 3A). This results in a tightly packed zigzag pattern (fig. S9A), with a spacing of twice the thickness of the endoderm-mesenchyme composite in both directions, in agreement with experiments. By using our experimental observations of nonuniform proliferation as guides, we incorporate non-uniform growth to this pattern by allowing the growth of spots of the endoderm in the zigzag

valleys, centered at the deepest points of the valleys, with lateral diameter six times the endoderm thickness. These spots are grown laterally until their diameter doubles during the simulation relative to areas of the endoderm outside the spots. This pattern of growth causes the zigzags to shift and twist so as to relocate the rapidly growing regions to the arms, similar to our clay model. As the spots relieve their growth strain at the arms, they form previllous bulges (Fig. 5E). Sliced plane views of this twisted pattern reveal their similarity to the corresponding experimental patterns (Fig. 5F); bulging peaks are rotated,

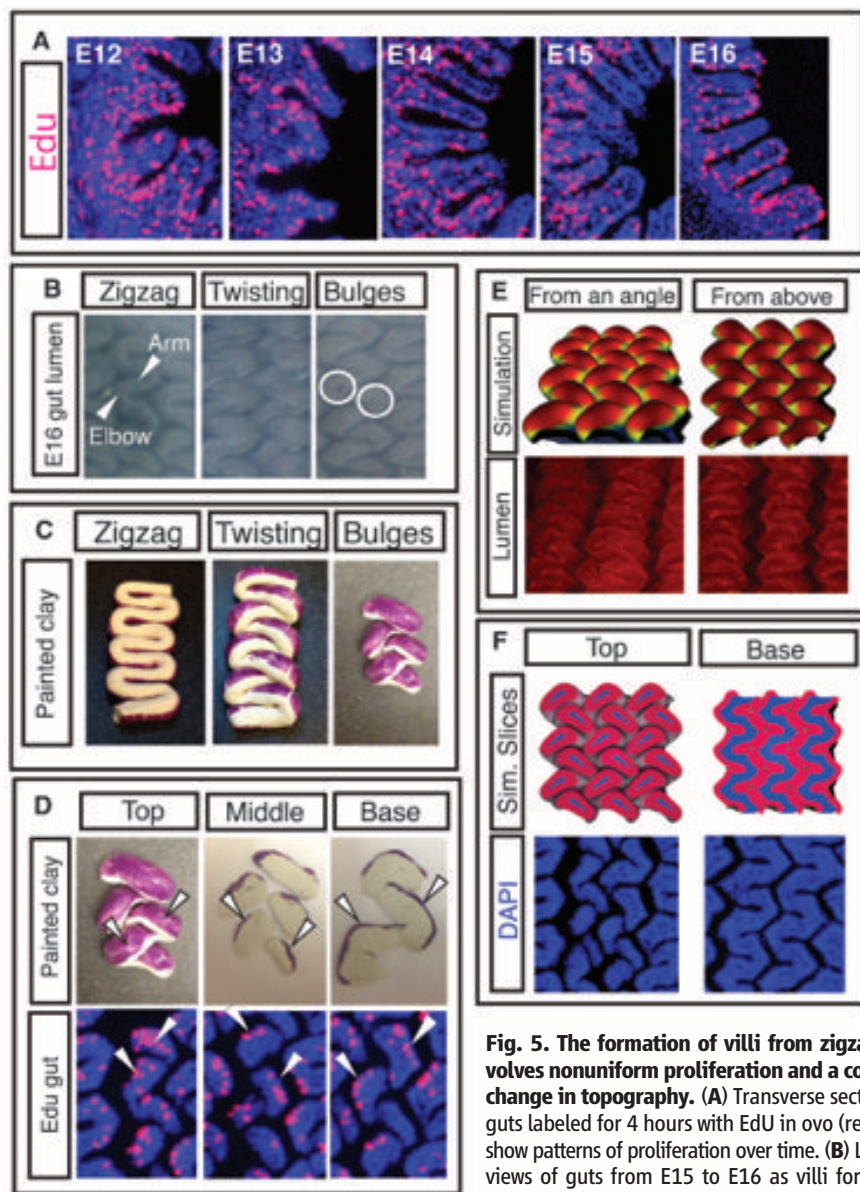


**Fig. 5. The formation of villi from zigzags involves nonuniform proliferation and a complex change in topography.** (A) Transverse sections of guts labeled for 4 hours with EdU in ovo (red) guts show patterns of proliferation over time. (B) Luminal views of guts from E15 to E16 as villi form. The "arm" of the zigzag rotates at the "elbow"; the circles denote the resulting pockets of mesenchyme surrounded by endoderm that will each become a villus. (C) Clay models; purple label represents proliferating regions. Clay model is twisted to mimic change in topography seen in (B). (D) (Top) Labeled, twisted model of E16 gut is sliced with a razor blade to reveal label localization. (Bottom) EdU label in longitudinal sections of E16 guts; arrowheads highlight similarity of pattern. (E) (Top) A simulation that incorporates nonuniform proliferation along with measured geometrical and biophysical parameters shows villi morphogenesis. (Bottom) Corresponding images of the chick lumen (red color and stained puncta are due to antibody stain and should be disregarded). (F) (Top) Sections of the simulations in (D). (Bottom) Corresponding sections in chick.

whereas the regular zigzag valleys persist deeper in the pattern.

Thus, although the final patterning step where definitive villi arise involves more complex morphogenesis and nonuniform proliferation, it follows from the same general physical principle: Differential growth in a constrained environment leads to buckling and folding patterns as circumferential, longitudinal, and eventually radial symmetry are broken sequentially.

### A Phylogenetically Conserved Mechanism Directs Luminal Gut Morphogenesis

Although the patterns seen on the luminal surface of the gut vary substantially across species (fig. S10), the underlying physical principles we have uncovered for the chick lumen morphology suggest that similar mechanisms operate broadly.

In the adult *Xenopus*, the luminal surface of the intestine is folded into a zigzag pattern (4). Development of this pattern involves progressing through the same patterning steps as in chick, with a smooth lumen forming ridges that then develop into zigzags via identical mechanisms (Fig. 6A). However, *Xenopus*, unlike chick, does not develop the second inner longitudinal muscle layer (Fig. 6A); the absence of this muscular layer, and thence the absence of additional compression, explains why individual villi do not develop in *Xenopus*. Our computational models can account for the differences in zigzags between *Xenopus* and chick, as well as more exotic patterns seen in snakes (supplementary materials and fig. S10).

In the mouse, the gut does not progress through ridges and zigzags; instead, villi emerge directly from a smooth lumen (20). Although these villi arise only once smooth muscle layers form, the layers differentiate much more rapidly in mouse than in chick (Fig. 6E). This suggests that the relatively quick pace at which muscle layers form in the mouse does not leave time for proliferation and expansion of the inner mesenchyme and endoderm between the differentiation of sequential muscle layers and thus prevents the development of visible intermediate patterns such as ridges and zigzags. Specifically, all muscle layers develop within a 48-hour period, a short time compared with the 8 days required for muscle to fully develop in chick (20). To experimentally determine whether villus formation in mouse also requires differentiation of smooth muscle, we tested the effect of the smooth muscle inhibitors used in our chick studies on the formation of villi in mouse guts grown in culture. Just as in chick, the mouse guts grown in the presence of AG1295 or FK506 did not form smooth muscle and concomitantly did not develop villi (Fig. 6B), suggesting that compression from the smooth muscle layer is necessary for, and drives the formation of, villi in mouse.

Our studies are in sharp contrast to a recent view of mouse gut patterning that postulates a potential inductive role of the endodermally derived signal Sonic hedgehog (Shh) in triggering

a morphogenetic cascade directing villus outgrowth (21). The key results that led in this direction were the failure of villus formation when Shh activity was pharmacologically blocked with the Shh antagonist cyclopamine and the increased size of the villi when guts were provided with excess Shh signal. However, because these reagents were applied before villus formation, they were de facto also treated before smooth muscle differ-

entiation. Because Shh activity is both necessary and sufficient to direct smooth muscle formation in the developing intestine (22, 23), an alternative explanation would be that cyclopamine, by preventing smooth muscle specification, eliminates the constraint necessary for villi to form, consistent with our current studies.

To quantitatively test our theory of villification in the mouse gut, we performed mechanical

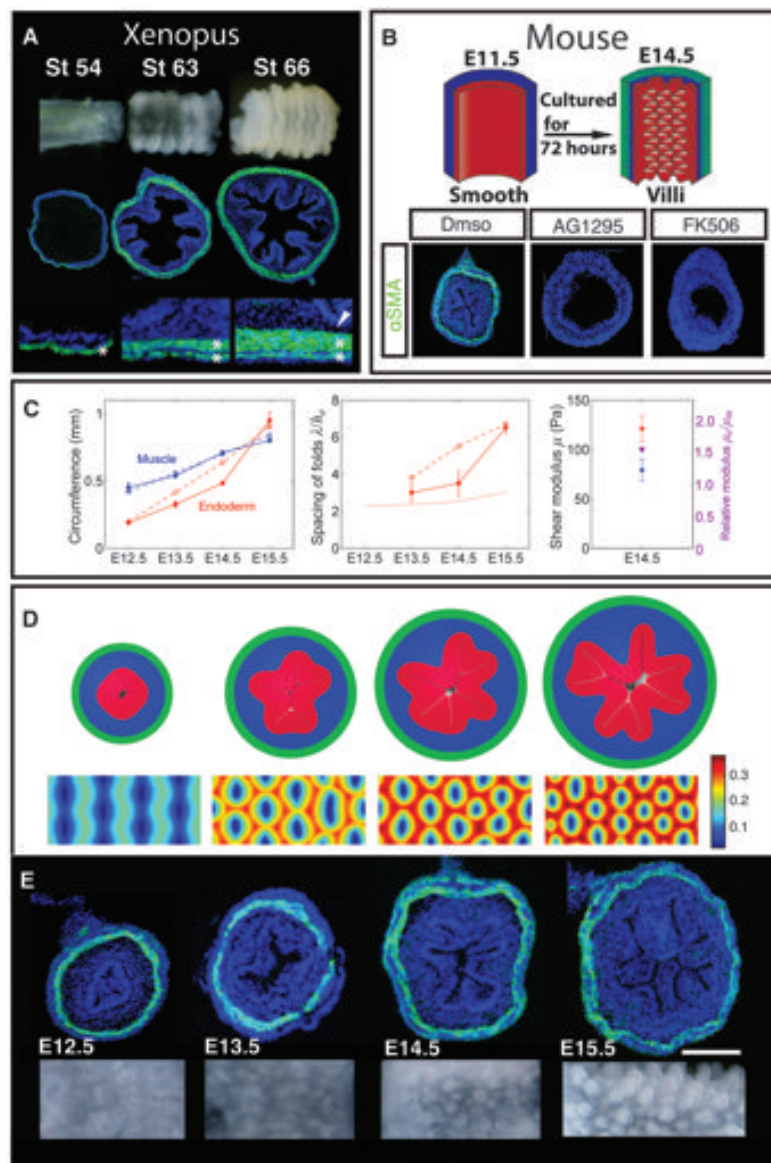


**Fig. 6. The physical mechanism of villification can be extended to other species.** (A) Luminal pattern formation in *Xenopus*. Sections labeled with DAPI (blue) and SMA (green). The circumferential and outer longitudinal layers form (asterisks), but the inner longitudinal layer does not form (arrowhead). (B) Transverse sections of E11.5 mouse guts [labeled as in (A)] cultured in vehicle alone (DMSO) or with either 10  $\mu$ M AG1295 or 10  $\mu$ M FK506 for 72 hours; experiment schematized above. (C) (Left) Circumference of the inner boundary of the muscle and endoderm. (Middle) Spacing of folds measured along the endoderm and scaled by its thickness. Dotted line is the stress-free thickness of the endoderm-mesenchyme composite. (Right) Shear moduli of mesenchyme and endoderm and their ratio. In all graphs, solid lines correspond to experimental observations and dashed lines to simulations. (D) Cross-sectional (top) and luminal (bottom) images from a simulation based on measurements from the developing mouse gut. Color shows distance of the luminal surface to the center line, relative to the diameter of the tube. (E) Transverse sections [labeled as in (A)] and whole-mount images of the lumen for corresponding stages during mouse villi formation.  $n > 3$  for culture experiments; error bars represent one SD. Scale bars = 100  $\mu$ m.



and morphometric measurements of the tissues in the developing mouse gut (Fig. 6C). Using these measurements as inputs in our model suffices to quantitatively predict the formation of villi (supplementary materials, Fig. 6D, and movie S3). Compared with the chick, where the endoderm is more than 10 times stiffer than the adjacent mesenchyme, the mouse endoderm is only about 1.5 times as stiff as the mesenchyme (fig. S3). Our simulations show that the soft endoderm in mouse is essential for the initial folding that occurs in endoderm alone and for the direct formation of an array of previllous bumps, rather than zig-zags, which are qualitatively similar to sulcus formation on biaxially compressed gel surfaces that lack a stiff top layer (24). The spacing of bumps and, consequently, the spacing of villi are comparable to the thickness of the whole endoderm-mesenchyme composite (Fig. 6C), similar to chick.

The process of villification occurs before the differentiation of the gut endoderm into various epithelial cell types (25–27) and well before the postnatal process of crypt formation. In vitro culture of intestinal stem cells results in the formation of intestinal organoids that reproduce crypt structure (28). These organoids consist of an inner epithelium with villuslike cell types and outwardly projecting cryptlike structures. However, no morphological structures are present in these in vitro cultures resembling the physical villi. These results suggest that crypt formation likely does not require the same muscle-driven compression that is necessary for villi to form.

Additionally, further study is needed to understand whether structural differences in the lumen of different regions of the gut are attributable to distinctions in the parameters we have measured. For example, the short, wide villi that coat large longitudinal folds of the chick colon may be attributable to the thicker muscle layers of the colon. Consistent with the muscle playing

such a role, studies have shown that transposition of a ring containing all radial layers of the colon into regions of the small intestine preserve villi morphology (29).

Our previous work provided a mechanical basis for the diversity of macroscopic looping patterns of the gut based on geometry, differential growth, and tissue mechanics (30), and our present results demonstrate that the same physical principles drive morphological variation on the luminal surface of the gut. Further, we see that relatively minor changes in the geometry, growth, and physical properties of the developing tissue in the guts of various species can substantially alter both the process and the form of villus patterning. A deep understanding of how patterns vary requires us to combine our knowledge of biophysical mechanisms with the genetic control of cell proliferation and growth; indeed this variation can occur in an organism as a function of its diet, across species, and over evolutionary time scales via natural selection.

#### References and Notes

1. V. A. McClint, S. J. Henning, M. Jamrich, *Gastroenterology* **136**, 2074–2091 (2009).
2. T. K. Noah, B. Donahue, N. F. Shroyer, *Exp. Cell Res.* **317**, 2702–2710 (2011).
3. W. J. Krause, *Anat. Histol. Embryol.* **40**, 352–359 (2011).
4. J. W. McAvoy, K. E. Dixon, *J. Anat.* **125**, 155–169 (1978).
5. S. Ferri, L. C. U. Junqueira, L. F. Medeiros, L. O. Medeiros, *J. Anat.* **121**, 291–301 (1976).
6. D. R. Burgess, *Embryol. Exp. Morph.* **34**, 723–740 (1975).
7. W. His, *Anatomie Menschlicher Embryonen* (Vogel, Leipzig, Germany, 1880).
8. D. E. Moulton, A. Goriely, *J. Mech. Phys. Solids* **59**, 525–537 (2011).
9. L. Bell, L. Williams, *Anat. Embryol.* **165**, 437–455 (1982).
10. M. Kurahashi et al., *Neurogastroenterol. Motil.* **20**, 521–531 (2008).
11. K. Fukuda, Y. Tanigawa, G. Fujii, S. Yasugi, S. Hirohashi, *Development* **125**, 3535–3542 (1998).
12. H. Benabdallah, D. Messaoudi, K. Gharzouli, *Pharmacol. Res.* **57**, 132–141 (2008).

13. N. Harada, Y. Chijiwa, T. Misawa, M. Yoshinaga, H. Nawata, *Life Sci.* **51**, 1381–1387 (1992).
14. M. L. Lovett, C. M. Cannizzaro, G. Vunjak-Novakovic, D. L. Kaplan, *Biomaterials* **29**, 4650–4657 (2008).
15. N. Bowden, S. Brittain, A. G. Evans, J. W. Hutchinson, G. W. Whitesides, *Nature* **393**, 146–149 (1998).
16. L. Mahadevan, S. Rica, *Science* **307**, 1740 (2005).
17. B. Audoly, A. Boudaoud, *J. Mech. Phys. Solids* **56**, 2444–2458 (2008).
18. E. Hannezo, J. Prost, J.-F. Joanny, *Phys. Rev. Lett.* **107**, 078104 (2011).
19. M. Ben Amar, F. Jia, *Proc. Natl. Acad. Sci. U.S.A.* **110**, 10525–10530 (2013).
20. R. Sbarbati, *J. Anat.* **135**, 477–499 (1982).
21. K. D. Walton et al., *Proc. Natl. Acad. Sci. U.S.A.* **109**, 15817–15822 (2012).
22. A. Sukegawa et al., *Development* **127**, 1971–1980 (2000).
23. M. Ramalho-Santos, D. A. Melton, A. P. McMahon, *Development* **127**, 2763–2772 (2000).
24. T. Tallinen, J. S. Biggins, L. Mahadevan, *Phys. Rev. Lett.* **110**, 024302 (2013).
25. M. Daga et al., *Int. J. Dev. Biol.* **34**, 205–218 (1990).
26. Z. Uni, A. Smirnov, D. Sklan, *Poult. Sci.* **82**, 320–327 (2003).
27. F. T. Bellware, T. W. Betz, *J. Embryol. Exp. Morphol.* **24**, 335–355 (1970).
28. T. Sato et al., *Nature* **459**, 262–265 (2009).
29. W. H. St. Clair, C. A. Stahlberg, J. W. Osborne, *Virchows Arch. B Cell Pathol. Incl. Mol. Pathol.* **47**, 27–33 (1984).
30. T. Savin et al., *Nature* **476**, 57–62 (2011).

**Acknowledgments:** We thank M. Kirschner for providing *Xenopus* tadpoles and O. Pourquie for providing snake embryos. D.L.K. and Tufts University hold a series of patents that cover the processing of silk into material structures, including those used in the research reported here. T.T. acknowledges the Academy of Finland for support. Computations were run at CSC—IT Center for Science, Finland. C.J.T. acknowledges the support of a grant from NIH R01 HD047360. L.M. acknowledges the support of the MacArthur Foundation.

#### Supplementary Materials

www.sciencemag.org/content/342/6155/212/suppl/DC1

Materials and Methods

Supplementary Text

Figs. S1 to S11

Movies S1 to S3

8 April 2013; accepted 13 August 2013

Published online 29 August 2013;

10.1126/science.1238842

## REPORTS

# Evidence for Water in the Rocky Debris of a Disrupted Extrasolar Minor Planet

J. Farihi,<sup>1\*</sup> B. T. Gänsicke,<sup>2</sup> D. Koester<sup>3</sup>

The existence of water in extrasolar planetary systems is of great interest because it constrains the potential for habitable planets and life. We have identified a circumstellar disk that resulted from the destruction of a water-rich and rocky extrasolar minor planet. The parent body formed and evolved around a star somewhat more massive than the Sun, and the debris now closely orbits the white dwarf remnant of the star. The stellar atmosphere is polluted with metals accreted from the disk, including oxygen in excess of that expected for oxide minerals, indicating that the parent body was originally composed of 26% water by mass. This finding demonstrates that water-bearing planetesimals exist around A- and F-type stars that end their lives as white dwarfs.

The enormous recent progress in the discovery of exoplanetary systems provides a growing understanding of their frequency

and nature, but our knowledge is still limited in many respects. There is now observational evidence of rocky exoplanets (1, 2), and the mass

and radius (and hence density) of these planets can be calculated from transit depth and radial velocity amplitude; however, estimates of their bulk composition remain degenerate and model-dependent. Transit spectroscopy offers some information on giant exoplanet atmospheres (3), and planetesimal debris disks often reveal the signature of emitting dust and gas species (4), yet both techniques only scratch the surface of planets, asteroids, and comets. Interestingly, white dwarfs—the Earth-sized embers of stars like the Sun—offer a unique window onto terrestrial exoplanetary systems: These stellar remnants can distill entire

<sup>1</sup>Institute of Astronomy, University of Cambridge, Cambridge CB3 0HA, UK. <sup>2</sup>Department of Physics, University of Warwick, Coventry CV5 7AL, UK. <sup>3</sup>Institut für Theoretische Physik und Astrophysik, University of Kiel, 24098 Kiel, Germany.

\*Corresponding author. E-mail: jfarihi@ast.cam.ac.uk



## Supplementary Materials for

### **Villification: How the Gut Gets Its Villi**

Amy E. Shyer, Tuomas Tallinen, Nandan L. Nerurkar, Zhiyan Wei, Eun Seok Gil, David L. Kaplan, Clifford J. Tabin,\* L. Mahadevan\*

\*Corresponding author. E-mail: [LM@seas.harvard.edu](mailto:LM@seas.harvard.edu) (L.M.); [Tabin@genetics.med.harvard.edu](mailto:Tabin@genetics.med.harvard.edu) (C.J.T.)

Published 29 August 2013 on *Science* Express

DOI: 10.1126/science.1238842

#### **This PDF file includes:**

Materials and Methods  
Supplementary Text  
Figs. S1 to S11

#### **Other Supplementary Material for this manuscript includes the following:**

available at [www.sciencemag.org/cgi/content/full/science.1238842/DC1](http://www.sciencemag.org/cgi/content/full/science.1238842/DC1)

Movies S1 to S3



# Materials and Methods

## Embryos and Dissections

Fertile chicken eggs (White Leghorn eggs) were obtained from commercial sources. All eggs were incubated at 37.5°C and staged according to the Hamburger and Hamilton protocols. Timed pregnant CD1 mice were obtained from Charles River. *Xenopus* embryos were derived by *in vitro* fertilizations and allowed to develop to the desired stages. The layers of the gut tube were separated using human hair, fine forceps, and tungsten wire to cut the connections between the layers.

## Immunohistochemistry and Edu Staining

Small intestines were collected from embryos at desired stages and fixed in 4% paraformaldehyde in PBS and embedded in OCT, allowing for 14µm transverse sections of the gut tube. Immunohistochemistry was performed with mouse anti-smooth muscle actin (FITC-conjugated, 1:200, Abcam), rabbit polyclonal anti-phospho-H3 (1:100, Millipore) overnight at 4 degrees in PBS containing 3% goat serum and 0.1% Triton X-100 (Davis, Kurpios et al. 2008). Sections were next incubated with Alexa Fluor 594 goat-anti-rabbit secondary antibody (1:300) for 1 hour at room temperature. DAPI (molecular probes) was used as a nuclear counter stain. 1mM Edu (Invitrogen) was injected in ovo and embryos were harvested 4 hours post-injection. Edu was detected in sectioned tissue using the Click-iT Edu system (Invitrogen).

## Organ Culture

Intestines were dissected from the embryos of the desired stage in cold PBS, connective tissue was removed, and intestines were gently pinned to an agar base with tungsten wire (for chick E6 or E12, mouse E11.5) or placed on transwells (Costar 3428) (for chick E15) in DMEM media supplemented with 1% pen/strep and 10% Chick Embryonic Extract (for chick tissue only). Intestines were cultured for 48 – 72 hours (as indicated in the figure legends) at 37°C with 5% CO<sub>2</sub> with media changes every 24 hr. E6 chick gut segments were drawn into silk tubes through mouth pipetting. AG1295 (EMD Biosciences) and FK506 (Sigma) were used at 10µM. SNP (Sigma) was used at 100µM and Motilin (Sigma) was used at 1µM. Frequency of peristaltic contraction was used to verify drug effectiveness. 0.5cm of gut segments were observed in culture for 1 minute: 5 to 9 contractions were observed in the control setting, 0 to 2 contractions were observed in the presence of SNP, and 15+ contractions were observed in the presence of Motilin.

## Measurement of tissue shear moduli

Layers of tissue gut were separated as described above, a ring of gut tissue comprised of either endoderm alone or endoderm and attached mesenchyme was placed in a dish of PBS between a glass cover slip, acting as a substrate, and a piece of glitter attached to a thin tungsten beam 0.004 inches in diameter and 4.12 inches in length, acting as a cantilever (Figure S3A). The ring of tissue is then compressed along its diameter through slow, measured movements of a micromanipulator attached to the tungsten beam (Figure S3A). Images were taken every 10µm after waiting one minute for the tissue to equilibrate. Measurements of the displacement of the glitter attached to the beam were attained by analyzing the resulting images with ImageJ. Plots of displacement of the glitter versus force (force = deflection of the beam × bending stiffness of the

beam) were created for each sample. The resulting data were incorporated into the model described below to determine the modulus of the sample. Five samples each of chick E8 and E10 and three samples of mouse E14.5 were measured to attain the modulus for each stage.

To be consistent with the experimental set-up to measure the shear moduli of different layers of chick/mouse gut, we construct the model for simulation as shown in Figure S3 using the mean values of geometric parameters measured from experiments. The gut samples, which are modeled as deformable cylindrical tubes, sit in between two rigid planes, the top one being the glitter and the bottom one being the substrate. The stiff layer is colored in green and the soft layer is colored in blue. We use a neo-Hookean constitutive equation to model the material behavior for both layers. Hard contact in the normal direction and frictionless sliding in the tangential direction are imposed as the contact conditions between the plane and outer surface of the tube. Only one eighth of the tube is simulated in practice by imposing symmetric boundary conditions on its symmetric planes. The simulated stiff section is meshed by  $50 \times 20 \times 40$  elements along the circumferential, the thickness and the length direction respectively, and the soft section is meshed by  $50 \times 30 \times 40$  in the corresponding directions. The reaction force on the top plane is recorded as a function of the displacement by which it is quasistatically compressed down for post analysis to get the shear moduli of both layers. In the simulation we first neglect any residual stresses that may be present in the endoderm-mesenchyme composite. Since the measurements were performed for layers separated from the muscle, the residual stresses were much smaller than those present in the compressed tubes, and the uncertainty attributed to them is small (see below). The simulation is conducted using the commercial finite element package ABAQUS 6.11.

The extraction of the shear modulus of the stiff layer from experimental data is straightforward, since for a given geometry and a neo-Hookean material, the reaction force on the glitter is linear in its shear modulus  $\mu$ . A test simulation with modulus  $\mu_0$  is run based on the model shown in Figure S3B, and thus  $\mu = c\mu_0$ , where the coefficient  $c$  is determined from the least-squares fitting between the simulation curve and the experimental data. Only first 5 to 8 points at which the compression displacement is relatively small are used for the numerical fit to determine  $c$  because in the strongly nonlinear regime (Fig. S3C, D), strain stiffening occurs in most polymeric materials and the neo-Hookean constitutive model is no longer valid. Figure S3 shows the comparison between the best-fit simulation and experimental curves, in which each experimental curve is averaged over 5 repeated measurements. We also fit those 5 individual measurements separately and then take the mean of the fitted moduli. The two results are almost identical. Knowing the modulus of the stiff layer, in order to get that of the soft layer, we compress the two layers together laterally as shown in Figure S3E. As the dependence of reaction force on the moduli of both layers is implicit, we have to repeat the simulation many times varying the modulus of the soft layer while keeping that of the stiff layer the same until the experimental data is enclosed by a narrow range of simulation curves with different moduli. Within this region, linear interpolation of curves with prescribed moduli is adopted to best match the experimental data by the least-squares fitting. Again, we fit both the averaged curve and the 5 individual measurements separately and then average the moduli. The two results are almost identical. Figure S3 H, I, J shows the results for chick gut at E8, E10 and mouse gut.

In order to test the effect of residual stress on modulus measurement, we set up a series of simulations as shown in Figs. S4 and S5. When we cut open the tube along the axial direction, if there is no residual stress or eigenstrain in the material, the tube should not deform at all and look exactly like an intact one (Fig. S4). However, when we apply a linearly varying residual strain, realized through an inhomogeneous temperature field leading to differential thermal expansion



(akin to relative growth), that is larger on the inner surface than on the outer surface the tube opens up to relax the differential expansion. Different amplitudes of the residual “eigenstrain” applied lead to different opening angles at equilibrium state, measured as shown in Fig. S4. This allows us to calibrate the role of the eigenstrains in terms of residual opening angle.

Then, we apply the same eigenstrain as in Fig. S4 to the intact tube (Fig. S5) and allow the tube to equilibrate, and perform a compression test by moving a rigid plane downwards quasistatically, just as the physical experiment. The compression distance and the reaction force on the rigid plane are both recorded as shown in Fig. S6. We can see that except when the eigenstrains correspond to the opening angles  $\alpha = 260.1^\circ$  and  $\alpha = 292.1^\circ$ , i.e. are very large, the curves collapse onto the one without eigenstrain. Using a least squares fit between the curves with different amplitude of eigenstrains, which we label by their corresponding opening angles, and the curve without eigenstrain to extract the effective shear moduli (Fig. S6) shows that the maximum increase in shear modulus when the eigenstrain is considered is around 15% at  $\alpha = 292.1^\circ$ . However, in the experiments, the opening angle is far smaller than  $\alpha = 292.1^\circ$ , so that the effect of residual stress on measuring the modulus is insignificant.

## Computational model of luminal patterns

When the endoderm-mesenchyme composite is surgically separated from the muscle, it expands and unfolds, releasing the luminal ridges. Furthermore, when the endoderm is peeled from the mesenchyme and cut open it relaxes to an approximately planar sheet. These observations suggest that the patterning is driven by mechanical instabilities and that the folded states are energy minima of an elastic endoderm-mesenchyme composite whose constituents grow uniformly, but at different rates, in a cylindrical volume constrained by a relatively much stiffer muscle. Our experimental observations show that this is true during development at least until approximately E14 or E15 in chick and mouse.

To investigate the folding patterns numerically, we construct a finite element model that minimizes the deformation energy of the system consisting of elastic mesenchyme and endoderm layers. The simulated layers are discretized into a rectangular mesh, and each rectangle is divided into five tetrahedron elements as indicated in Figs. S11. Arrangement of the tetrahedrons in any two neighboring rectangles is reflected in order to preserve the reflection symmetries of the mesh. The mesh spacing is denoted by  $a$ . We note that this model is a full custom implementation, in contrast to the Abaqus model that we used above for the modulus measurements.

A stress-free state of an elemental tetrahedron is characterized by the matrix

$$\mathbf{G} = [\hat{\mathbf{x}}_1 \quad \hat{\mathbf{x}}_2 \quad \hat{\mathbf{x}}_3],$$

where  $\hat{\mathbf{x}}_1$ ,  $\hat{\mathbf{x}}_2$  and  $\hat{\mathbf{x}}_3$  are vectors describing the tetrahedron (Fig. S11D). The stress-free state grows and changes shape (if growth is anisotropic) so as to describe the growth of the tissue. The deformed state of the tetrahedron is contained in

$$\mathbf{A} = [\mathbf{x}_1 \quad \mathbf{x}_2 \quad \mathbf{x}_3] = \mathbf{F}\mathbf{G},$$

where  $\mathbf{x}_1$ ,  $\mathbf{x}_2$  and  $\mathbf{x}_3$  are the deformed basis vectors (Fig. S11E) and  $\mathbf{F}$  is the elastic deformation gradient. At each time step of the simulation  $\mathbf{F}$  is obtained by

$$\mathbf{F} = \mathbf{A}\mathbf{G}^{-1}.$$

We note that this decomposition is different from the typically used multiplicative decomposition of the deformation gradient as the product of the elastic and growth deformations, as we just use the experimentally measured stress-free states and their variation as a function of time to deduce  $\mathbf{G}$  and thence proceed. Mechanically, this is similar to most previous works where differential growth or residual stresses are modeled (for example, in arteries, see Holzapfel et al. *J. Elasticity* **61**, 1-48 (2000)). We model the tissues by a neo-Hookean constitutive model with strain energy density

$$W = \frac{\mu}{2} [\text{Tr}(\mathbf{F}\mathbf{F}^T)J^{-2/3} - 3] + K(J - \log J - 1),$$

where  $\mu$  and  $K$  are the shear and bulk moduli, respectively, and  $J = \det(\mathbf{F})$ . We assume compressible material with  $K = 3\mu$  in all simulations due to the long timescales involved in villification. Experimentally, the compressibility of the tissues becomes evident when the mesenchyme-endoderm composite is separated from the muscle; it expands in volume as is obvious from Fig. 2A. In contrast, we assumed incompressible material in determining the elastic moduli (see above), as the moduli measurements were performed in much shorter timescale. The Cauchy stress corresponding to  $W$ , i.e., the force per unit area in the deformed state is given by

$$\boldsymbol{\sigma} = \frac{1}{J} \frac{\partial W}{\partial \mathbf{F}} \mathbf{F}^T.$$

Force acting on each deformed face ( $i = 1, 2, 3, 4$ ) of the tetrahedron is given by

$$\mathbf{s}_i = -\boldsymbol{\sigma} \mathbf{n}_i,$$

where  $\mathbf{n}_i$  are normals with lengths proportional to the deformed areas of the faces. Nodal forces are obtained by distributing the force acting on each face equally to its three vertices.

Since the deformations of the lumen are large, they often lead to self-contact, so that our model must also include these effects. Element faces at the surface make up a triangular lattice for which self-avoidance can be enforced by processing vertex-triangle and edge-edge contacts. Contacts are penalized by energy  $Ka^2[(h - d)/h]^2$  if the separation  $d$  between a vertex and triangle, or between two edges, is less than the contact range  $h = a/3$ . Contact force from this potential is interpolated to the nodes of the associated geometric primitives.

After the nodal forces are determined, we solve damped Newton's equations of motion while varying the growth parameters as given from experiments. This algorithm is implemented using the following explicit scheme for the integration of the equations of motion:

$$\mathbf{v}(t + \Delta t) = \mathbf{v}(t) + \frac{\mathbf{f}(t) - \gamma \mathbf{v}(t)}{m} \Delta t,$$

$$\mathbf{x}(t + \Delta t) = \mathbf{x}(t) + \mathbf{v}(t + \Delta t) \Delta t.$$

Here  $\Delta t = 0.1a/\sqrt{K}$  is the time step,  $m = a^3$  mass of a node, and  $\gamma = 10m$  viscous damping factor. Vectors  $\mathbf{f}$ ,  $\mathbf{v}$  and  $\mathbf{x}$  are force, velocity and position of a node, respectively. The simulations are allowed to equilibrate fully at every stage.



### Details for the tubular chick and mouse simulations for the formation of luminal ridges, zigzags and bumps (Figs. 4 and 6 in the main article)

To model the relative growth in the mesenchyme-endoderm tubes, growth is parameterized in terms of  $t \in [0,1]$  so that the dimensions of the mesenchyme and endoderm are varied as a function of  $t$  so as to approximate the observed geometries. In both simulations mesenchyme and endoderm are restricted into a cylindrical tube with diameter  $D$  and length  $L = 1.25D$ . The outer boundary of the mesenchyme is clamped to the cylinder and periodic boundary conditions are applied at the ends of the tube. Stress-free states of the mesenchyme and endoderm are assumed to correspond to flat sheets, consistent with observations, i.e. if separated and cut open they would relax into flat sheets.

These simulations are implemented in reverse order, that is, the tube and layers with dimensions corresponding to  $t = 1$  are first equilibrated and then  $t$  is taken from 1 to 0, with dimensions of the layers changing as described below. Performing the simulations in the direction of real time yields qualitatively similar results, but with slightly fewer folds and higher deformation energies, i.e., the tube may get trapped in metastable states. Either way the simulation is run, the number of folds shifts spontaneously, but the simulated configurations are not strictly guaranteed to be in the state of global energy minimum. In principle, similar trapping to local energy minima occur also in real systems. However, the mechanical environment in real guts likely involves perturbations (e.g., from muscle contractions etc.) that aid in crossing weak local minimums. We thereby resort to running simulations shown in Figs. 4 and 6 backward in time, since it yields lower deformation energies and thus more realistic appearance.

For the chick gut simulation (Fig. 4) the simulation mesh, including both layers, has  $400 \times 160 \times 24$  rectangles (width  $\times$  length  $\times$  thickness).  $D$  increases linearly by a factor 2.7 from  $t = 0$  to  $t = 1$ , corresponding to real time going from E7 to E14. The endoderm is 12 times stiffer than the mesenchyme ( $\mu_e/\mu_m = 12$ ), i.e., we neglect the small difference in the measured modulus between E8 and E10, see Figs. 4A and S3. The stress-free dimensions (see Fig. S11F) of the endoderm are taken to be: thickness  $h_e = (0.13 - 0.1t)D$ , width (circumferential)  $w_e = (0.35 + 2.8t - 1.4t^2)\pi D$  and length (longitudinal)  $l_e = (1 + 0.5t^2)L$ . The stress-free dimensions of the mesenchyme are taken to be: thickness  $h_m = (0.39 - 0.3t)D$ , width (circumferential)  $w_m = 1.5\pi D$  and length (longitudinal)  $l_m = (1 + 0.333t^2)L$ .

For the mouse gut simulation (Fig. 6) the simulation mesh, including both layers, has  $320 \times 160 \times 30$  rectangles (width  $\times$  length  $\times$  thickness).  $D$  increases linearly by a factor 2.0 from  $t = 0$  to  $t = 1$ , corresponding to real time going from E12.5 to E15.5. The endoderm is 1.5 times stiffer than the mesenchyme ( $\mu_e/\mu_m = 1.5$ ). The stress-free dimensions (see Fig. S11F) of the endoderm are taken to be: thickness  $h_e = (0.2 - 0.1t)D$ , width (circumferential)  $w_e = (0.5 + 2t - t^2)\pi D$  and length (longitudinal)  $l_e = (1.6 + 1.2t - 0.6t^2)L$ . The stress-free dimensions of the mesenchyme are taken to be: thickness  $h_m = (0.2666 - 0.0666t)D$ , width (circumferential)  $w_m = 1.5\pi D$  and length (longitudinal)  $l_m = (1.4 + 0.8t - 0.4t^2)L$ .

The above dimensions of the stress-free states are chosen so as to approximately yield the observed cross-sectional geometries and expansion ratios of separated mesenchyme-endoderm composite. Although there is some variability in the estimation of the stress-free geometries of the different tissue types, especially those of the mesenchyme, our simulations suggest that the folding is not very sensitive to the exact stress-free state of the mesenchyme. Furthermore, the coarse residual strain measurement of the mesenchyme on a few samples indicates that the above stress-free states are realistic, so that our results are robust to small variations in these parameters.

### Details for the zigzag simulation (Fig. 5 in the main article)

The effect of non-uniform growth on a zigzag pattern is investigated by simulating a small planar domain that contains one zigzag cell (visualizations in Fig. 5 and Fig. S9A show nine replicates of the simulated domain). The domain has periodic lateral boundaries and a clamped base. The mesh size is  $120 \times 120 \times 32$  rectangles (width  $\times$  length  $\times$  thickness), and the stiffness of the endoderm is assumed to be larger than that of the mesenchyme and related to it via the expression  $\mu_e/\mu_m = 12$  consistent with our measurements for chick (Fig. S3). The stress-free thickness of the endoderm is  $h_e = h_m/2$ .

The simulation starts from a zigzag pattern that is created by growing the endoderm laterally such that its stress-free width  $w_e = 2W$  and length  $l_e = 2L$ , where  $W$  and  $L$  are the lateral dimensions of the simulation domain. The mesenchyme is grown laterally as well such that its dimensions  $w_m = 1.666W$  and  $l_m = 1.666L$ . The lateral dimensions of the simulation domain are optimized to minimize the energy of the pattern, which yields  $W \approx L = 2.0(h_e + h_m)$ . This result is in agreement with the approximately equal circumferential and longitudinal spacing of the zigzags in real chick guts.

The flat stress-free state of the endoderm is broken by laterally expanding spots that are centered in the pits of the zigzag pattern, i.e., the points of the endoderm that are nearest to the base (Fig. S9B). For parameterized time going from  $t = 0$  (uniformly compressed state) to  $t = 1$ , the relative expansion of a spot is given by  $1 + (e^{-\eta} - 0.2)t$  with  $\eta = [r/(3h_e)]^2$ , where  $r$  is the distance from the origin of the spot along the endoderm in the stress-free state before the expansion. This form of expansion keeps the total stress-free area of the endoderm approximately constant due to the negative expansion far from the spots. The total expansion includes superposed contributions of both spots in the simulation domain. As a result the whole zigzag valley expands, with the most expansion at the pits (Fig. S9C). Lateral dimensions of the simulation domain and the stress-free state of the mesenchyme are held fixed during this step.

The applied growth field here only qualitatively mimics the experimental observations, since it is difficult to determine the actual growth field. In addition to proliferation, movement of cells relative to each other may contribute in the process of moving from a flat to non-flat stress-free state. Nevertheless, the simulation robustly captures the twisting and rotation of the zigzags that precede the formation of definite villi. Interestingly, this transformation breaks the longitudinal reflection symmetry of the pattern, despite the initial zigzag pattern as well as the applied growth field have the longitudinal reflection symmetry.

### Simulations with stretched mesenchyme (Fig. S10)

In chick and mouse both the mesenchyme and endoderm grow faster than the constraining muscular layers. This means that both layers are under compression, which leads to ridges and zigzags separated by sharply fold valleys. In contrast, if mesenchyme grows at a lower rate than the muscular layers, the mesenchyme has to stretch with the growing tube and it gets under tension. Our simulations indicate that this changes the appearance of the folding patterns; the valleys become wider as the mesenchyme tension is increased. We illustrate this in the simulations shown in Fig. S10. In the cylindrical simulation of Fig. S10B the mesenchyme is stretched by a factor of 1.5 in circumferential and longitudinal directions, while the endoderm (we assume  $\mu_e = 10\mu_m$ ) is still under compression; its stress-free circumference is 1.666 times the circumference of the tube, and its stress-free length is 1.333 times the length of the tube. The simulated configuration displays features similar to African house snake, including the clearly separated zigzags that appear flat-topped in the cross-section images.

With higher mesenchyme tension these effects become more pronounced. In Fig. S10C we compare simulated folding patterns in a planar setting to the luminal patterns observed in Wagler's snake. In the simulation, the mesenchyme is stretched by a factor of two in both directions, and the compression of the endoderm is varied by growing its stress-free dimensions first in one planar direction and then to the other. The stiffness of the endoderm is again  $\mu_e = 10\mu_m$ , and the thickness  $h_e = h_m/3$ . As the endoderm buckles, we see condensation of the buckles into narrow ridges (lower panel of Fig. S10C). When growth of the endoderm in the other planar direction sets in, ridges perpendicular to that direction arise, similar to the proximal snake gut (upper panel of Fig. S10C), although the present simulation does not capture similar hexagonal arrangements of the ridges.



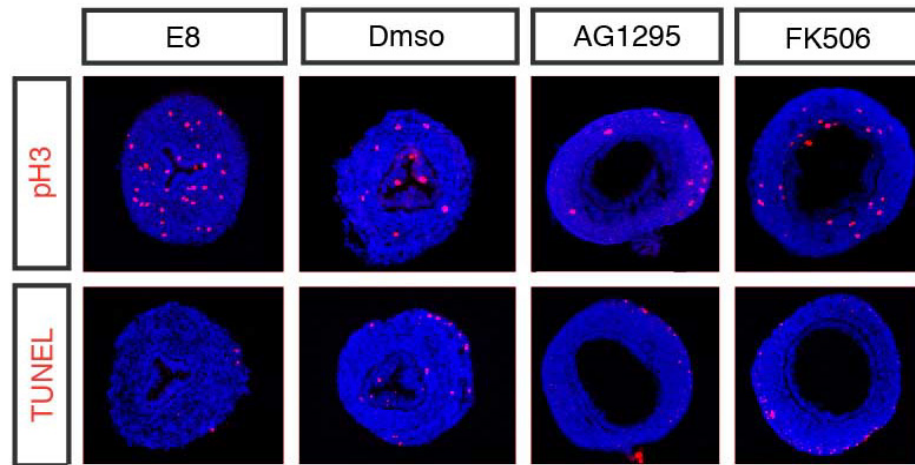


**Figure S1: AG1295 and FK506 do not impact proliferation or cell death.** E6 chick gut segments were grown in culture for 48 hours, compare with guts collected from E8 embryos, left. While levels of proliferation (top) are lower *in vitro* than to *in vivo*, gut segments cultured in the presence of either AG1295 or FK506 do not display significantly altered proliferation when compared to segments grown in drug vehicle alone. Additionally, while there is slightly more cell death (bottom) in guts grown *in vitro* than *in vivo*, segments grown in the presence of either drug do not exhibit more cell death than those grown in vehicle alone.

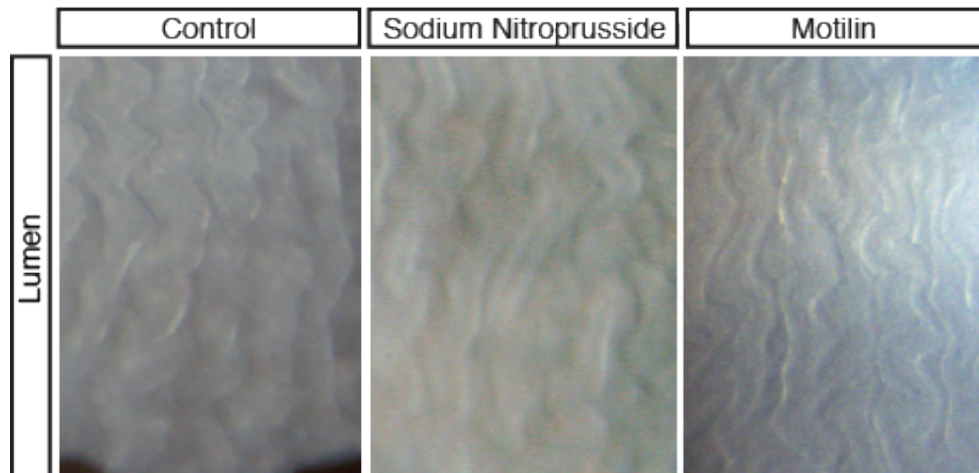


**Figure S2: Peristaltic contraction is not involved in the formation of zigzags.** E12 guts were cultured with either sodium nitroprusside or Motilin or no drug (control). Although sodium nitroprusside inhibits contraction and Motilin stimulates contraction, in all cases zigzags begins to form.

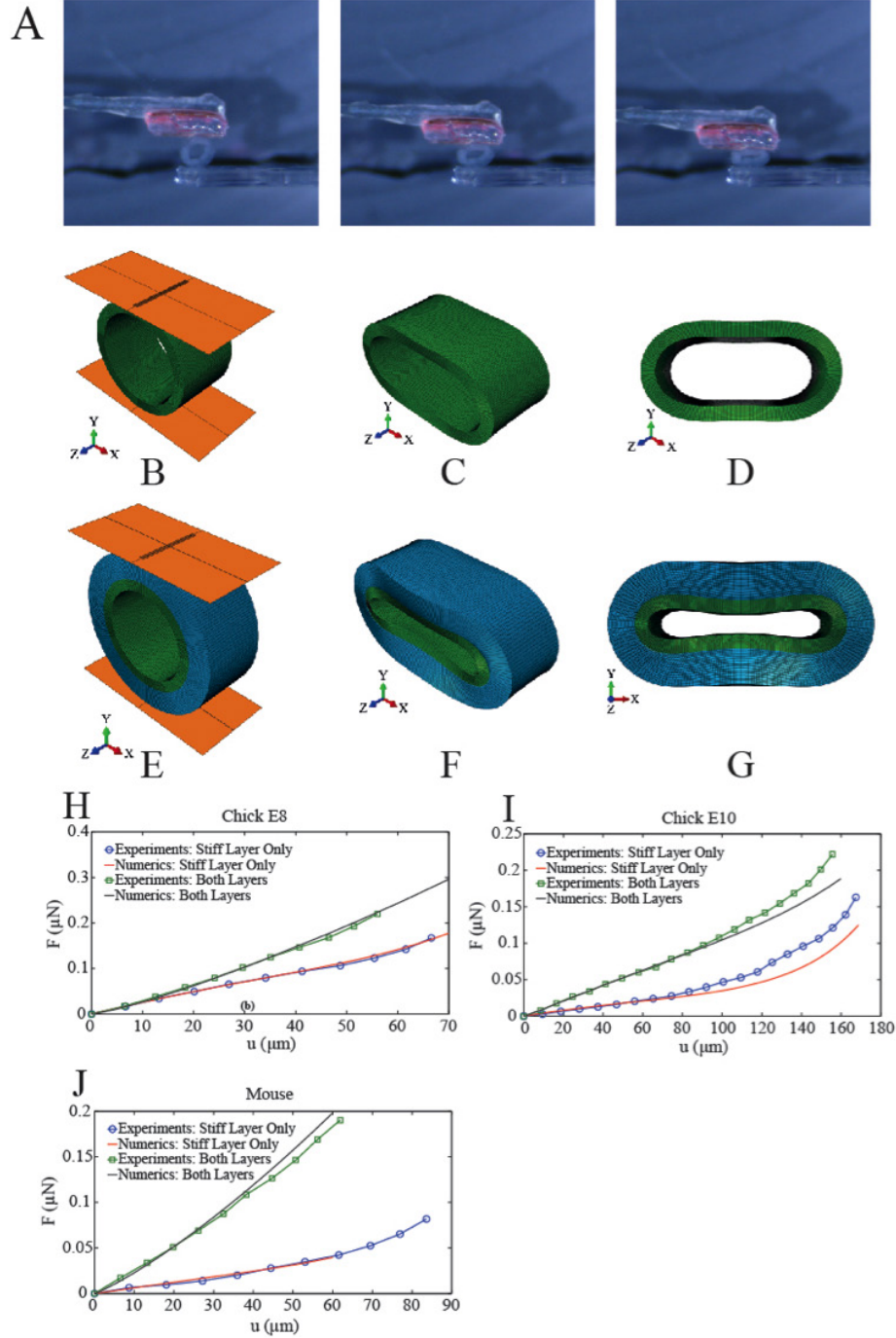


**Figure S3: Simulation for measurement of shear modulus.** (A) Examples of images used to measure modulus. A sample of E10 chick endoderm and mesenchyme is shown (left to right) as the glitter (top of images, pink) is incrementally moved towards the coverslip (bottom of image, clear). (B) Modeled compression of only the stiff layer for chick E10. (C) and (D) are views from different angles of the final deformed stiff layer. (E) Compression of both layers for chick E10. The stiff layer is green and the soft layer is blue. (F) and (G) are views from different angles of the final deformed state. Reaction force versus displacement compressed downwards from both experiments and least-squares fitting for (H) chick E8 (first 7 points are used for fitting), (I) chick E10 (first 8 points are used for fitting), (J) mouse (first 5 points are used for fitting).

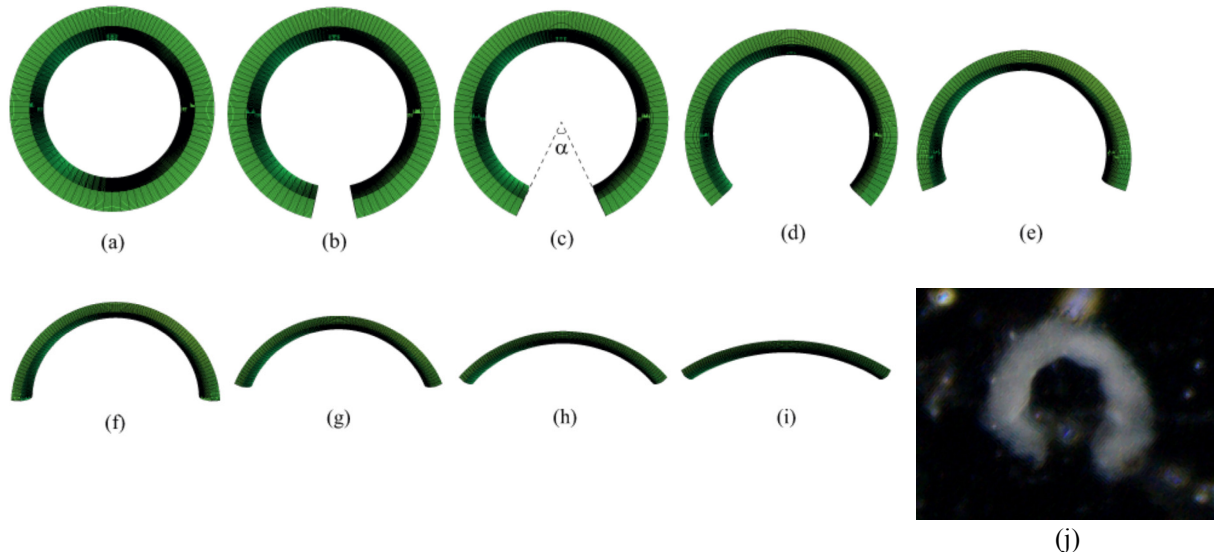


**Figure S4:** (a) A short tube without residual strain, when cut, does not open. When a linearly varying eigenstrain (the inner strain larger than the outer strain) is applied on the tube across the thickness direction, shown in (b)- (i), and the tube is cut along the axis, it opens up to relax the stress. The amplitude of the eigenstrain increases from (b) to (i) so that the opening angle also increases, from (b)  $\alpha = 24.3^\circ$  (c)  $\alpha = 48.2^\circ$ , (d)  $\alpha = 94.9^\circ$ , (e)  $\alpha = 140.0^\circ$ , (f)  $\alpha = 183.2^\circ$ , (g)  $\alpha = 223.5^\circ$ , (h)  $\alpha = 260.1^\circ$ , (i)  $\alpha = 292.1^\circ$ . (j) E10 endoderm-mesenchyme composite ring, cut open to view the opening angle, shows that there is a residual strain in the system.

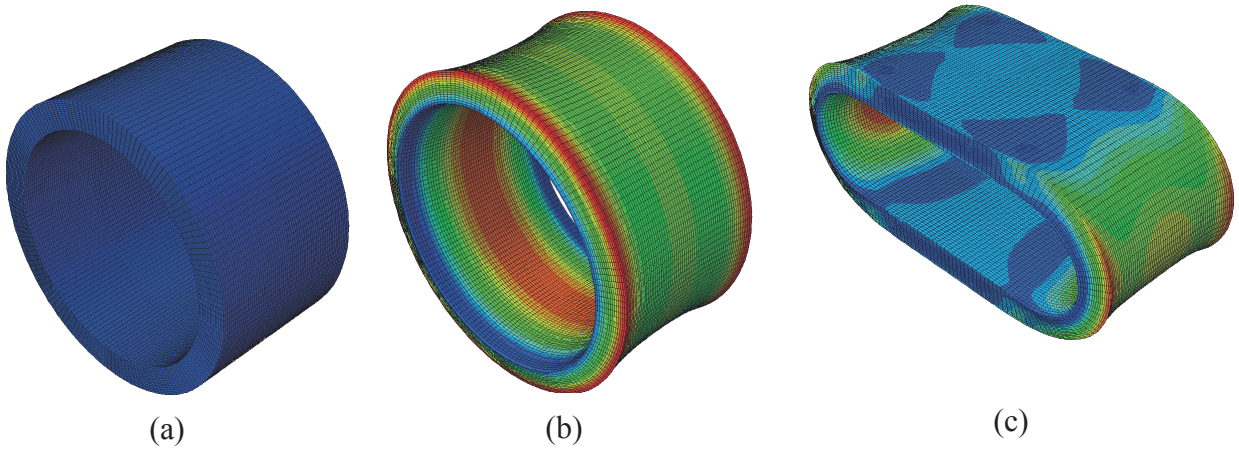
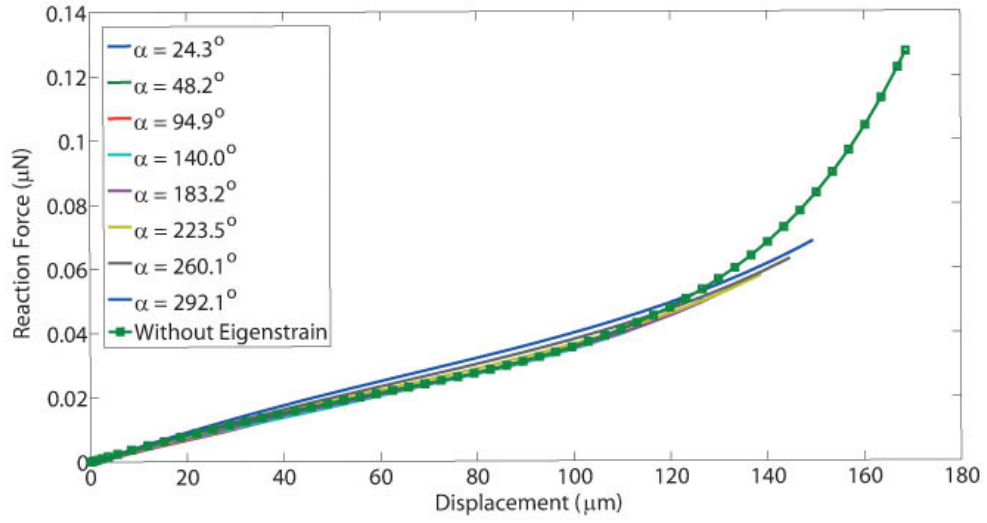
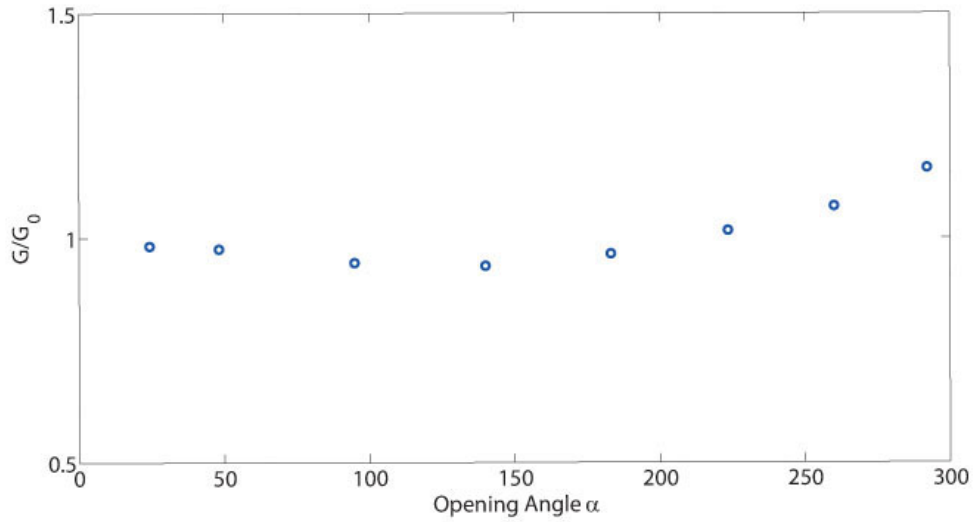


**Figure S5:** (a) An intact tube that has no residual strain in its natural state. (b) The corresponding eigenstrain shown in Fig. S4b-i when applied to (a), causes the tube, when equilibrated to have a slightly deformed state. (c) The final compressed state mimicking the experimental protocol shown in Fig. S3.





(a)



(b)

**Figure S6: The role of the eigenstrain on the shear modulus.** (a) The force as a function of the compressive displacement, corresponding to Fig. S5c. (b) The dimensionless shear modulus as a function of opening angle which reflects the amplitude of the eigenstrain shows a very weak dependence on the residual eigenstrain. Here  $G_0$  is the shear modulus when the eigenstrain is absent.

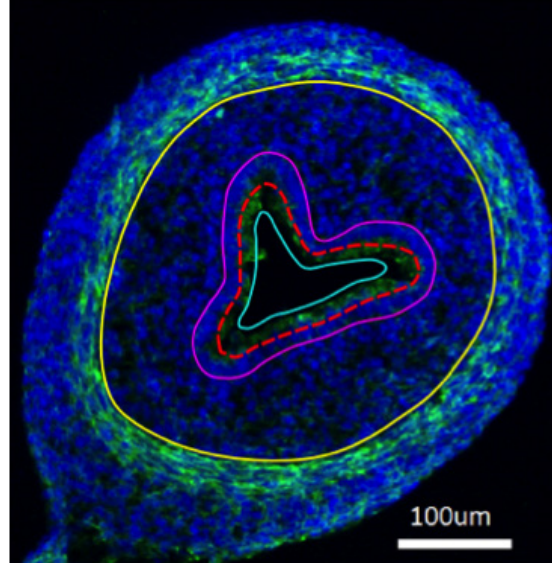


**Figure S7: Segmentation of a cross-section.** Solid lines show the outer circumference  $S_0$  of the mesenchyme (yellow), outer circumference of the endoderm (magenta) and inner circumference of the endoderm (cyan). The dashed red line is the mean circumference  $S_e$  of the endoderm that is plotted in Figs. 4A and 6C. Thickness of the deformed endoderm can be approximated as the area occupied by the endoderm divided by  $S_e$ . All geometric measurements shown in Figs. 4A and 6C are averages of measurements of three different guts, and the error bars are the standard-deviations of these three independent measurements for each point. The geometric measurements are performed with ImageJ.

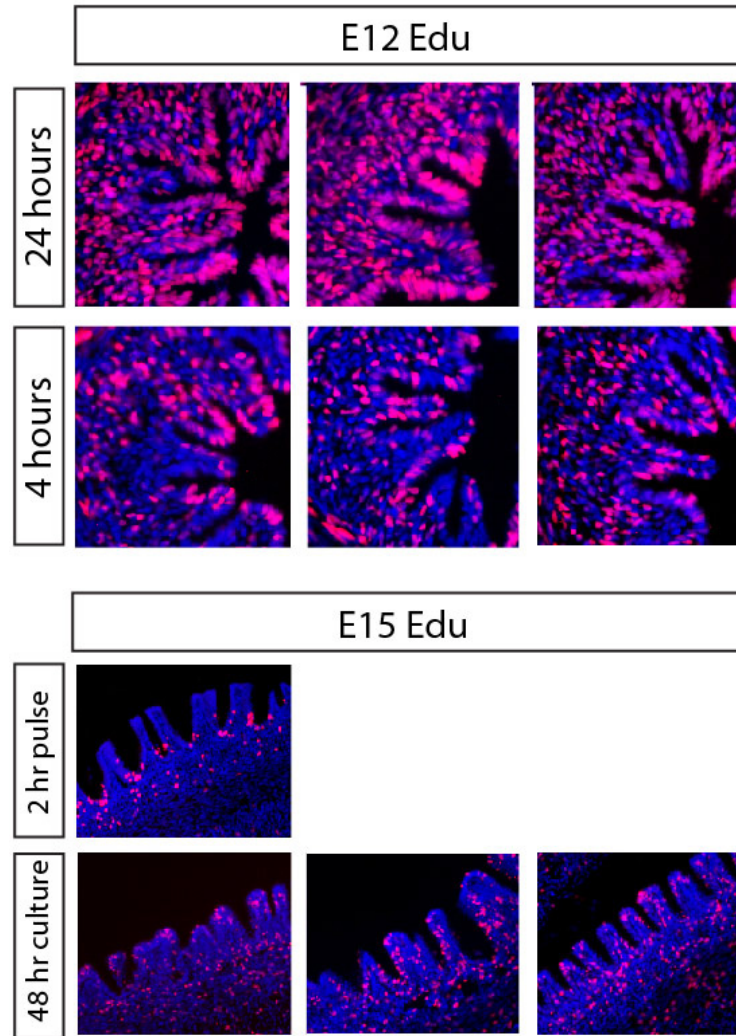


**Figure S8: Patterns of proliferation before and after villi formation.** Top - Edu labels nearly all cells at E12 when 3 pulses are applied at 3 hour intervals *in ovo* and tissue is collected 24 hours after first pulse. Unlike at E15 where Edu is clearly restricted from the distal aspects of the tissue, patterns of proliferation are not visible after 4 hours of *in ovo* Edu labeling at E12. Shown here are 3 additional representative images equivalent to those shown in Figure 5. Bottom – E15 gut segments were pulsed with 10 $\mu$ m Edu *in vitro* for 2 hours. Tissue samples were collected directly after the pulse to reveal the pattern of labeled cells before villi form and also after 48 hours in culture (lower panels). After 48 hours, labeled cells are found along the length and at the tip of forming villi, pointing to relocation of cells from the base to the tips as villi form.



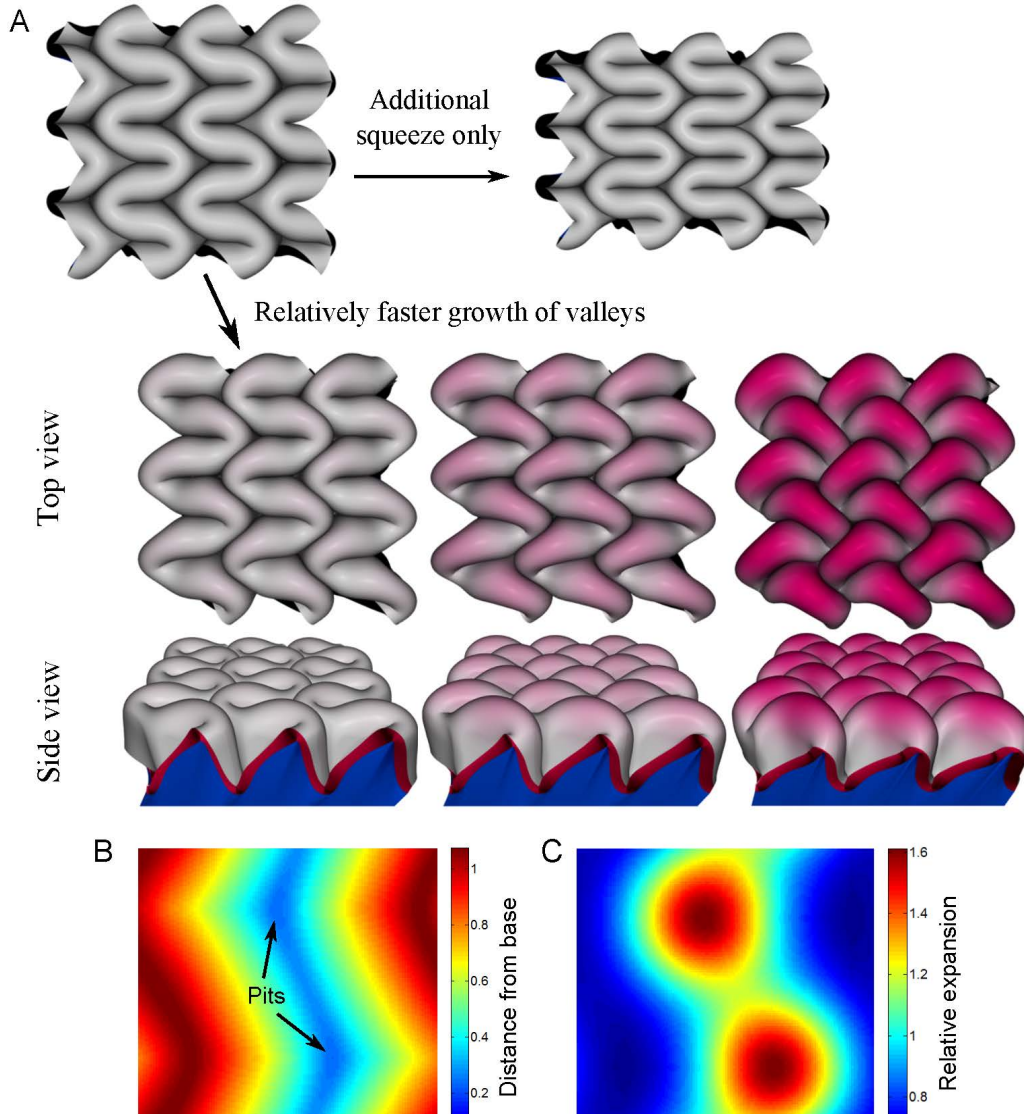


**Figure S9: Localized growth of a zigzag pattern leads to twisting and bulging of arms.** (A) A zigzag pattern resulting from uniform growth is shown top left. With additional longitudinal compression the zigzags only squeeze, preserving the up/down reflection symmetry. The cascade on bottom (top and side views) shows the twisting and up/down symmetry breaking due to enhanced growth of the valleys (parameterized time  $t = 0.5$ ,  $0.75$ , and  $1$  from left to right). The applied growth map is shown in C for  $t = 1$ . The growth map is based on the depth map of the original zigzag pattern (B) such that peak growth occurs at the zigzag pits. Purple areas in simulation snapshots have the highest expansion, corresponding to the maxima in the growth map and minima in the height map of the original untwisted pattern.

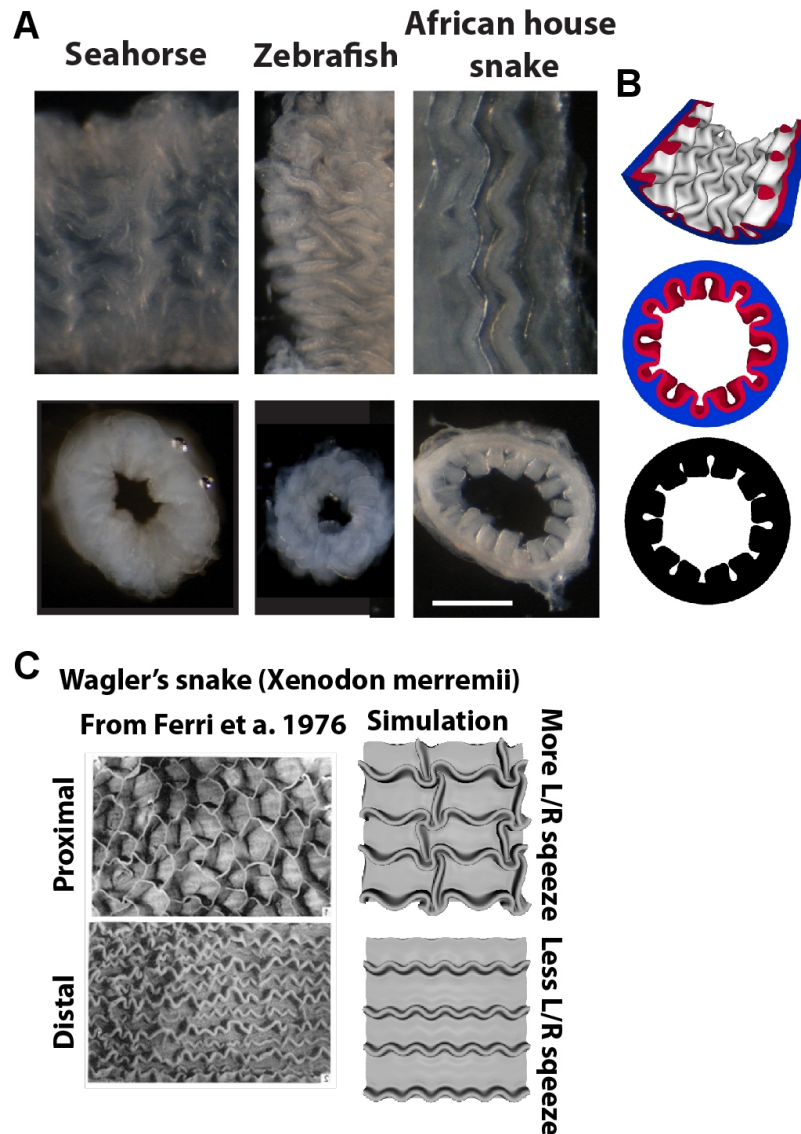


**Figure S10: The patterns seen on the luminal surface of the gut vary across species.** (A) Luminal views (top) and cross sectional view (bottom) of guts of various species. The adult seahorse gut (left) has disorganized zigzags with lateral extensions. The adult zebrafish gut (middle) has short zigzagging protrusions that are oriented laterally. The African house snake gut at E55 shortly before hatching (right) has tall flat zigzags. Scale bar represents 500µm. (B) Tall flat zigzags in African house snake can be mimicked in simulations by placing the mesenchyme under tension, which leads to widened valleys between the folds. Images show luminal view (top), cross-sectional view of a short longitudinal segment (middle), and a silhouette of the middle image (bottom), that reveals why the folds may appear having flat tops. (C) Snake guts show morphologies with very wide flat valleys between the folds. They can be mimicked in simulations by placing the mesenchyme under strong tension. Note proximal intestine has hexagonal ridges, which turn in to zigzags in the distal intestine. This transition can be modeled by adding more relative longitudinal (shown L to R) growth in the endoderm of the proximal model and less in the distal model.

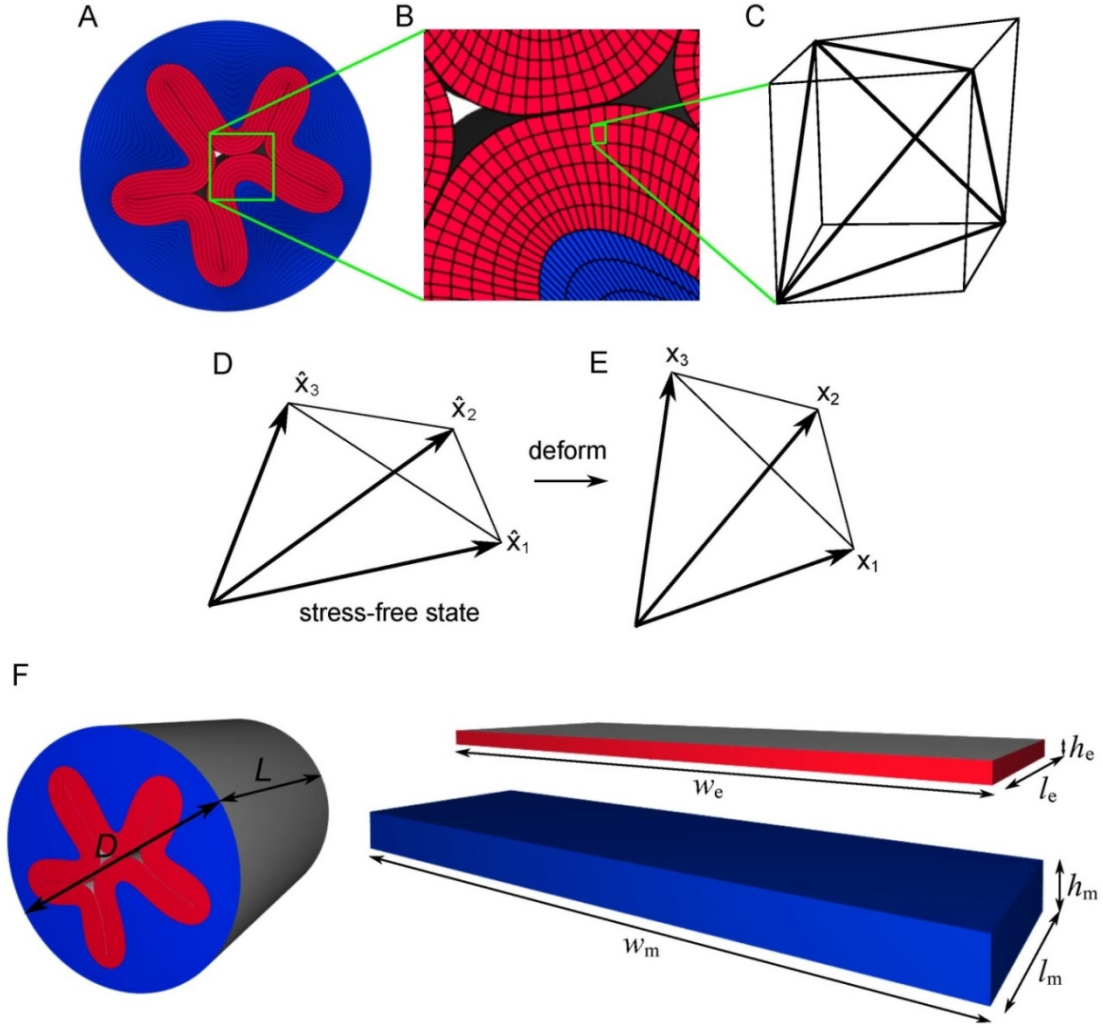


**Figure S11: Computational model for the mesenchyme-endoderm tube.** (A) A composite of elastic mesenchyme (blue) and endoderm (red) layers is squeezed into a cylindrical tube. (B) A magnified view of the deformed mesh. (C) A schematic of a primitive rectangle showing the arrangement of its five tetrahedrons. Schematic stress-free and deformed states of a tetrahedron are shown in D and E, respectively. (F) The diameter  $D$  and length  $L$  of the compressed tube are indicated on left, and the stress-free states of the layers are shown on right with their dimensions indicated.



## Movie captions

Movie S1: Simulated growth of a chick gut, corresponding to Fig. 4C.

Movie S2: Twisting of zigzags, corresponding to Figs. 5E and S9. The first half of the movie shows twisting of a zigzag pattern resulting from non-uniform growth. The latter half shows sliced plane view going through the final state of the simulation.

Movie S3: Simulated growth of a mouse gut, corresponding to Fig. 6D.